

## Quarterly Technical Report

## Solid State Research

2002:4

---

**Lincoln Laboratory**  
MASSACHUSETTS INSTITUTE OF TECHNOLOGY  
*LEXINGTON, MASSACHUSETTS*

---



Prepared for the Department of the Air Force under Contract F19628-00-C-0002.

Approved for public release; distribution is unlimited.

20030508 175

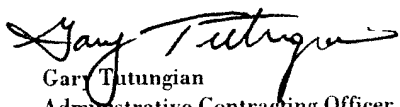
This report is based on studies performed at Lincoln Laboratory, a center for research operated by Massachusetts Institute of Technology. The work was sponsored by the Department of the Air Force under Contract F19628-00-C-0002.

This report may be reproduced to satisfy needs of U.S. Government agencies.

The ESC Public Affairs Office has reviewed this report, and it is releasable to the National Technical Information Service, where it will be available to the general public, including foreign nationals.

This technical report has been reviewed and is approved for publication.

FOR THE COMMANDER

  
Gary Tutungian  
Administrative Contracting Officer  
Plans and Programs Directorate  
Contracted Support Management

Non-Lincoln Recipients

PLEASE DO NOT RETURN

Permission is given to destroy this document  
when it is no longer needed.

Massachusetts Institute of Technology  
Lincoln Laboratory

**Solid State Research**

**Quarterly Technical Report**  
**2002:4**

1 August — 31 October 2002

Issued 11 April 2003

Approved for public release; distribution is unlimited.

## **ABSTRACT**

This report covers in detail the research work of the Solid State Division at Lincoln Laboratory for the period 1 August through 31 October 2002. The topics covered are Quantum Electronics, Electro-optical Materials and Devices, Submicrometer Technology, Biosensor and Molecular Technologies, Advanced Imaging Technology, Analog Device Technology, and Advanced Silicon Technology. Funding is provided by several DoD organizations—including the Air Force, Army, DARPA, MDA, Navy, NSA, and OSD—and also by the DOE, NASA, and NIST.

This Page Intentionally  
Left Blank

## TABLE OF CONTENTS

Abstract	iii
List of Illustrations	vii
List of Tables	xi
Introduction	xiii
Reports on Solid State Research	xv
Organization	xxvii
 1. QUANTUM ELECTRONICS	
1.1 Laser-Induced Breakdown Spectroscopy for the Detection and Classification of Biological Aerosols	1
 2. ELECTRO-OPTICAL MATERIALS AND DEVICES	
2.1 Wafer-Bonded Internal Back-Surface Reflectors for Enhanced GaInAsSb/GaSb TPV Performance	5
2.2 Geiger-Mode InGaAsP/InP Avalanche Photodiodes for Photon Counting at 1.06 $\mu\text{m}$	10
2.3 Advances in Thermoelectric Materials and Devices Using Molecular Beam Epitaxy, Thermoelement Arrays, and Novel On-Chip Characterization	15
 3. SUBMICROMETER TECHNOLOGY	
3.1 Diamond Optically Switched Schottky Diodes	21
3.2 X-Ray Zone Plate Fabrication	24
 4. BIOSENSOR AND MOLECULAR TECHNOLOGIES	
4.1 Cell and Assay Analyses in CANARY Biosensor Development	27
 5. ADVANCED IMAGING TECHNOLOGY	
5.1 Deep-Depletion Image Sensors	31

6. ANALOG DEVICE TECHNOLOGY

6.1 Domain Wall Motion Effects on High-Frequency Permeability of Ferrites	35
---	----

7. ADVANCED SILICON TECHNOLOGY

7.1 Low-Temperature Oxide-Bonded Three-Dimensional Integrated Circuits	39
--	----

## LIST OF ILLUSTRATIONS

Figure No.		Page
1-1	Representative single-shot laser-induced breakdown spectra of aerosolized samples. Although the spectra are taken from a single shot and charge-coupled device exposure, the aerosol cloud was sufficiently concentrated that multiple particles contribute to each spectrum.	2
1-2	Three-dimensional scatter plot of entire data set in the principal component analysis (PCA) coordinates. Each plot symbol represents a single spectrum acquired from a single laser shot. The principal components were computed using three linear combinations of the intensities of 29 lines from the spectra. Each class of bioaerosol contains three different types, e.g., the mold category is composed of penicillium, corn smut, and oat smut.	3
1-3	PCA plots of each bioaerosol class where the principal components were determined from training sets comprising average spectra of each specific type of bioaerosol. In all three cases the first two principal components account for >95% of the training set's variance.	4
2-1	Schematic structure of (a) inverted GaInAsSb/GaSb thermophotovoltaic (TPV) device structure grown on <i>n</i> -GaSb substrate for wafer bonding, and (b) wafer-bonded GaInAsSb/GaSb TPV structure on GaAs handle wafer after removal of GaSb substrate and InAsSb etch-stop layer.	6
2-2	Measured reflectivity of SiO <sub>x</sub> /Au reflector with various SiO <sub>x</sub> thicknesses on GaAs.	7
2-3	Interferograms of (a) back side of GaSb substrate bonded to GaAs handle substrate, and (b) back side of GaAs handle substrate. One fringe corresponds to 4.8 μm.	8
2-4	X-ray diffraction of (a) control GaInAsSb/GaSb TPV wafer and (b) wafer-bonded GaInAsSb/GaSb TPV structure.	9
2-5	300-K photoluminescence of control and wafer-bonded GaInAsSb/GaSb TPV structures.	9
2-6	Reflectivity spectrum of uncoated and antireflection-coated wafer-bonded GaInAsSb/GaSb TPV structure. The TPV device structure is 4 μm thick. Thinner device layers will increase the resonant fringe spacing.	10



## LIST OF ILLUSTRATIONS (Continued)

Figure No.		Page
2-7	(a) Drawing of layer design and mesa structure of avalanche photodiode (APD), and micrographs showing (b) single detector and (c) $4 \times 4$ detector array.	12
2-8	Overbias dependence of photon detection efficiency and dark count rate in $33\text{-}\mu\text{m}$ -diam detectors from wafer 1 and wafer 2 at room temperature.	13
2-9	Temperature dependence of dark count rate at 2-V overbias for $37\text{-}\mu\text{m}$ -diam detectors from three wafers.	14
2-10	Image recorded in indoor 60-m range with $4 \times 4$ array of InGaAsP/InP Geiger-mode APDs in the Gen I Ladar system.	14
2-11	Electron microscope image of tetrahedral PbSe quantum dots on the surface of PbTe.	16
2-12	Electron microscope image of individual thermoelements obtained by metallization and etching.	16
2-13	Comparison between conventional co-linear and new non-co-linear transmission line techniques for determination of specific electrical contact resistance.	18
3-1	Current-voltage curve of Schottky diode taken in the dark. The dashed curve (in the high forward conduction state) starting at $-200\text{ V}$ was taken after exposing the diode to uv light. When the bias voltage reached $985\text{ V}$ , the diode was illuminated with incandescent light. The light was turned off and the voltage was stepped back from $1000$ to $-200\text{ V}$ , as shown by the solid line. The inset is an optical micrograph of $\sim 9\text{ }\mu\text{m}$ of an epitaxial diamond layer on a $4 \times 4\text{-mm}$ type Ib diamond substrate. The rough surface is the result of polishing damage in the original diamond substrate growing into the epitaxial layer. The central square region is a Schottky diode consisting of $50\text{ nm}$ of Cr patterned into a $100 \times 100\text{-}\mu\text{m}$ square.	22

## LIST OF ILLUSTRATIONS (Continued)

Figure No.		Page
3-2	<p>Acceptor density under the Schottky diode as determined by capacitance-voltage measurements. The solid curve, for a diode in the conductive state, was obtained after the diode was exposed to uv light. The dashed curve, for the same diode in the insulating state, where the active acceptor density is <math>&lt;10^{13} \text{ cm}^{-3}</math>, was obtained after being biased to 1000 V and exposed to incandescent light. The pictorial insert shows two drawings of an epitaxial layer on a type Ib diamond substrate, contacted with a Schottky diode. (a) Schottky diode in the conducting state where the diamond substrate contains no positive charge and the epitaxial layer contains neutral (<math>B^0</math>) and ionized (<math>B^-</math>) boron atoms and mobile holes (<math>e^+</math>). (b) Schottky diode in the insulating state where the substrate contains positively charged nitrogen atoms (<math>N^+</math>) and no mobile holes in the epitaxial layer.</p>	23
3-3	Scanning electron micrograph of 45-nm-wide outer zones of zone plate patterned in polymethyl methacrylate (PMMA) resist.	25
3-4	Process flow for zone plate fabrication with a trilayer resist: (a) pattern PMMA imaging layer, (b) etch Ti using PMMA mask, (c) etch thick polymer layer using Ti mask to form mold, and (d) plate gold into polymer mold.	25
4-1	(a) Dry impaction concept and (b) prototype device. Inexpensive single-use impactors are envisioned that would include a downstream filter to prevent contamination of the (reusable) air pump that maintains the air flow through the impactor. This design is readily scalable for parallel collection into multiple commercial off the shelf (COTS) tubes.	27
4-2	(a) Response to 500 000 colony-forming units of <i>Yersinia pestis</i> with B cells desiccated using different additives (dried on agarose, with glycan and glycerol, or with no additives), stored for nine days at room temperature, rehydrated, and primed and loaded for the CANARY assay; (b) dose response of B cells treated with DMSO, dried on agarose, and stored for two days at room temperature before rehydration and preparation for assay; and (c) response of B cells prepared for assay before desiccation and stored for two days.	29

## LIST OF ILLUSTRATIONS (Continued)

Figure No.		Page
5-1	Depiction of cross section of charge-coupled device (CCD) showing depletion layer edges on low- and high-resistivity substrates.	32
5-2	Illustration of substrate isolation issues at the perimeter of a device.	32
5-3	Measurement of hole current from device channel stops to substrate for various values of bias on the two inner guard rings.	33
5-4	Depletion depth as a function of substrate bias from capacitance-voltage measurements on a special test pattern that represents the CCD pixel array.	34
6-1	Model of domain wall displacement under the influence of a longitudinal ac magnetic drive field.	36
6-2	Schematic diagram of permeability variations as a function of frequency caused by various magnetic damping actions.	38
7-1	Concentric via cross section. This design requires only one mask as compared with the three used in earlier work [1].	40
7-2	Surface energy of bonded wafer pairs as measured by the blade insertion/crack propagation method.	41
7-3	Arrhenius plot of surface energy vs bonding temperature for 1- and 10-h cycles. Data from [4] is shown as the dashed line.	41
7-4	Percentage of bonded wafer area covered by voids as a function of bonding temperature.	42
7-5	Scanning electron micrograph cross section of concentric vias in an oxide-bonded structure. The via etch created a sloped profile above the holes in the metal that were not completely filled with tungsten, producing "Y" shaped plugs in cross section.	43
7-6	Plot of mean via resistance and range for three-tier via chains. Via size refers to the width of the opening in the top metal.	43
7-7	Photograph of section of a three-dimensional (3D) ring oscillator. The W plug concentric via process was not used for this device.	44
7-8	Gate delay vs voltage for a 65-stage ring oscillator fabricated in 0.8- $\mu\text{m}$ CMOS with 3- $\mu\text{m}$ 3D vias.	45

## LIST OF TABLES

Table No.		Page
4-1	Dry-Impacted Aerosol Samples Analyzed with the CANARY Assay	28

This Page Intentionally  
Left Blank

## INTRODUCTION

### 1. QUANTUM ELECTRONICS

Laser-induced breakdown spectra (LIBS) of a set of bioaerosol materials have been recorded to evaluate the potential of LIBS as a bioaerosol sensor. Initial results indicate high discrimination and classification capability between common types of bioaerosols.

### 2. ELECTRO-OPTICAL MATERIALS AND DEVICES

Epitaxial layers of GaInAsSb/GaSb thermophotovoltaic (TPV) device structures have been wafer bonded to a GaAs wafer with an internal reflector for enhanced performance. The structural and optical properties of the wafer-bonded TPV device layers were maintained after fabrication, and since the back-surface reflector provides electrical isolation of the TPV device layers, GaInAsSb TPV devices could be monolithically interconnected.

InGaAsP/InP Geiger-mode avalanche photodiodes (APDs) designed for sensitive photon-counting performance at 1.06  $\mu\text{m}$  have been developed. Arrays of these APDs have been tested as focal planes in a three-dimensional imaging laser radar (Ladar) system.

New techniques have been developed for the preparation of molecular beam epitaxy-grown advanced arrays for thermoelectric cooling and power generation applications. A novel technique for transmission-line measurement of the specific contact resistance allows on-chip characterization during device processing in real time.

### 3. SUBMICROMETER TECHNOLOGY

A novel optically switched diamond device has been demonstrated. Charge exchange between the diamond substrate and the epitaxial layer makes it possible to modulate the conductivity of the epitaxial layer, and once the layer conductivity has been established it will remain in the same electrical state for days, if kept in the dark.

X-ray zone plate optics with 45-nm features have been patterned using scanning electron beam lithography. These zone plates have demonstrated better than 80-nm imaging resolution in a commercial x-ray microscope.

### 4. BIOSENSOR AND MOLECULAR TECHNOLOGIES

In the development of the CANARY (Cellular Analysis and Notification of Antigen Risks and Yields) biosensor, background contamination resistance has been studied using a dry aerosol collection device. In addition, analyses have been performed on ready-to-use B cells that have been frozen and stored for extended periods and on B cells that have been desiccated using different additives prior to storage.

## **5. ADVANCED IMAGING TECHNOLOGY**

A method of increasing the depletion depth of image sensors without raising circuit voltages has been demonstrated, in which the use of certain device design guidelines allows the substrate to be electrically isolated from the imager circuits, which in turn allows it to be biased independently of the imager. Capacitance-voltage measurements on a charge-coupled device-like test structure made on 6900  $\Omega\cdot\text{cm}$   $p$ -type silicon show depletion depths greater than 150  $\mu\text{m}$ , or more than a factor of 2 higher than without substrate bias.

## **6. ANALOG DEVICE TECHNOLOGY**

The issue of domain wall effects on high-frequency permeability of ferrites has been studied. Domain wall resonance is analyzed, and its influence on permeability contrasted with the effects of single-domain rotation and gyromagnetic resonance.

## **7. ADVANCED SILICON TECHNOLOGY**

Three-dimensional integrated circuits have been fabricated using a low-temperature oxide bonding technique that can be applied to completed circuit wafers. Two-tier silicon-on-insulator CMOS circuits had operational ring oscillators, and three-tier concentric via chains were functional at sizes as small as 1.5  $\mu\text{m}$ .

**REPORTS ON SOLID STATE RESEARCH**  
**1 AUGUST THROUGH 31 OCTOBER 2002**

**PUBLICATIONS**

- |   |   |   |
|---|---|---|
| Contamination Rates of Optical Surfaces at 157 nm in the Presence of Hydrocarbon Impurities | T. M. Bloomstein<br>V. Liberman<br>M. Rothschild<br>S. T. Palmacci<br>D. E. Hardy<br>J. H. C. Sedlacek                                | <i>Proc. SPIE 4691</i> (Pt. 1), 709<br>(2002)                 |
| Modeling of Acid Catalyzed Resists with Electron Beam Exposure                              | T. H. Fedynyshyn<br>J. R. Gillman<br>R. B. Goodman<br>T. M. Lyszcza<br>S. J. Spector<br>D. M. Lennon<br>S. J. Deneault<br>R. H. Bates | <i>Proc. SPIE 4690</i> (Pt. 2), 1126<br>(2002)                |
| Fluoraromatic Resists for 157-nm Lithography  | T. H. Fedynyshyn<br>R. R. Kunz<br>R. F. Sinta<br>M. Sworin<br>W. A. Mowers<br>R. B. Goodman<br>A. Cabral                              | <i>J. Photopolym. Sci. Technol.</i> <b>15</b> ,<br>655 (2002) |
| High Resolution Fluorocarbon Based Resist for 157-nm Lithography                            | T. H. Fedynyshyn<br>W. A. Mowers<br>R. R. Kunz<br>R. F. Sinta<br>M. Sworin<br>R. B. Goodman   | <i>Proc. SPIE 4690</i> (Pt. 1), 29<br>(2002)                  |



157 nm Pellicles: Polymer Design  
for Transparency and Lifetime

R. H. French\*  
R. C. Wheland\*  
W. Qiu\*  
M. F. Lemon\*  
G. S. Blackman\*  
E. Zhang\*  
J. Gordon\*  
V. Liberman  
A. Grenville\*  
R. R. Kunz  
M. Rothschild

*Proc. SPIE* **4691** (Pt. 1), 576  
(2002)

Behavior of Candidate Organic  
Pellicle Materials under 157 nm  
Laser Irradiation

A. Grenville\*  
V. Liberman  
M. Rothschild  
J. Gordon\*  
E. Zhang\*  
R. C. Wheland\*  
R. H. French\*  
J. H. C. Sedlacek

*Proc. SPIE* **4691** (Pt. 2), 1644  
(2002)

Quantum Dot Superlattice  
Thermoelectric Materials and  
Devices

T. C. Harman  
P. J. Taylor  
M. P. Walsh  
B. E. LaForge

*Science* **297**, 2229 (2002)

Recent Developments in the  
Characterization of  
Superconducting Films by  
Microwaves

M. A. Hein\*  
M. Getta\*  
S. Kreiskott\*  
B. Mönter\*  
H. Piel\*  
D. E. Oates  
P. J. Hirst\*  
R. G. Humphreys\*  
H. N. Lee\*  
S. H. Moon\*

*Physica C* **372-376** (Pt. 1), 571  
(2002)

---

\*Author not at Lincoln Laboratory.

Long-Term Laser Durability  
Testing of Optical Coatings and  
Thin Films for 157-nm Lithography

V. Liberman  
M. Rothschild  
S. T. Palmacci  
N. N. Efremow  
J. H. C. Sedlacek

*Proc. SPIE* **4691** (Pt. 1), 568  
(2002)

Attenuating Phase Shifting Mask at  
157 nm

V. Liberman  
M. Rothschild  
S. J. Spector  
K. E. Krohn  
S. G. Cann  
S. Hein\*

*Proc. SPIE* **4691** (Pt. 1), 561  
(2002)

GaAsP/InP Avalanche Photodiodes  
for Photon Counting at 1.06  $\mu\text{m}$

K. A. McIntosh  
J. P. Donnelly  
D. C. Oakley  
A. Napoleone  
S. D. Calawa  
L. J. Mahoney  
K. M. Molvar  
E. K. Duerr  
S. H. Groves  
D. C. Shaver

*Appl. Phys. Lett.* **81**, 2505  
(2002)

Nonlinear Microwave Surface  
Impedance of YBCO Films: Latest  
Results and Present Understanding

D. E. Oates  
M. A. Hein\*  
P. J. Hirst\*  
R. G. Humphreys\*  
G. Koren\*  
E. Polturak\*

*Physica C* **372-376** (Pt. 1), 462  
(2002)

---

\*Author not at Lincoln Laboratory.

Flux-Based Superconducting  
Qubits for Quantum Computation

T. P. Orlando\*  
S. Lloyd\*  
L. S. Levitov\*  
K. K. Berggren  
M. J. Feldman\*  
M. F. Bocko\*  
J. E. Mooij\*  
C. J. P. Harmans\*  
C. H. van der Wal\*

*Physica C* **372-376** (Pt. 1), 194  
(2002)

Resolution Enhancement of 157 nm  
Lithography by Liquid Immersion

M. Switkes  
M. Rothschild

*Proc. SPIE* **4691** (Pt. 1), 459  
(2002)

Investigation of the Physical and  
Practical Limits of Dense-Only  
Phase Shift Lithography for Circuit  
Feature Definition

B. M. Tyrrell  
M. Fritze  
R. D. Mallen  
B. D. Wheeler  
P. Rhyins\*  
P. Martin\*

*Proc. SPIE* **4692**, 503 (2002)

Third-Order Intermodulation  
Distortion in  $\text{YBa}_2\text{Cu}_3\text{O}_{7-\delta}$  Grain  
Boundaries

H. Xin  
D. E. Oates  
G. Dresselhaus\*  
M. S. Dresselhaus\*

*Phys. Rev. B* **65**, 214533-1–  
214533-5 (2002)

## PRESENTATIONS<sup>†</sup>

Periodically Poled BaMgF<sub>4</sub> for  
Ultraviolet Frequency Generation

S. C. Buchter\*  
T. Y. Fan  
V. Liberman  
J. J. Zayhowski  
M. Rothschild  
A. Cassanho\*  
H. P. Jenssen\*  
E. J. Mason  
H. H. Burnett\*

14th American Conference on  
Crystal Growth and Epitaxy,  
Seattle, Washington,  
4-8 August 2002

---

\*Author not at Lincoln Laboratory.

<sup>†</sup> Titles of presentations are listed for information only. No copies are available for distribution.

Effect of Growth Interruption on the Interfacial Quality of GaSb/GaInAsSb/AlGaAsSb Heterostructures Grown by Organometallic Vapor Phase Epitaxy	C. A. Wang D. A. Shiau C. J. Vineis* D. R. Calawa	14th American Conference on Crystal Growth and Epitaxy, Seattle, Washington, 4-8 August 2002
Demonstrations of High-Speed Superconductive Electronics	K. K. Berggren	Applied Superconductivity Conference, Houston, Texas, 4-9 August 2002
Processing Technology for Integrated Quantum-Information Storage, Measurement, and Control Circuitry	K. K. Berggren E. Macedo R. Slattery T. Weir D. Nakada* T. Orlando*	Applied Superconductivity Conference, Houston, Texas, 4-9 August 2002
Improved Critical Current Density Uniformity by Using Anodization	D. Nakada* K. K. Berggren E. Macedo V. Liberman T. Orlando*	Applied Superconductivity Conference, Houston, Texas, 4-9 August 2002
Tunable Superconducting Filters	D. E. Oates	Applied Superconductivity Conference, Houston, Texas, 4-9 August 2002
Microwave Nonlinearities from Resonant Absorption in MgO	D. E. Oates S-H. Park M. A. Hein* P. J. Hirst* R. G. Humphreys*	Applied Superconductivity Conference, Houston, Texas, 4-9 August 2002

---

\*Author not at Lincoln Laboratory.

Intermodulation Distortion and Third Harmonic Generation in YBCO Films of Varying Oxygen Content	D. E. Oates S-H. Park P. J. Hirst* R. G. Humphreys*	Applied Superconductivity Conference, Houston, Texas, 4-9 August 2002
Subwavelength Optical Lithography Using Resolution Enhancement Technology	M. Fritze	Gordon Research Conference on Nanostructure Fabrication, Tilton, New Hampshire, 4-9 August 2002
Photolithography Beyond 193 nm	M. Rothschild T. M. Bloomstein T. H. Fedynyshyn R. R. Kunz V. Liberman	15th IEEE Lithography Workshop, Kohala Coast, Hawaii, 12-16 August 2002
Immersion Lithography in the Deep Ultraviolet	M. Switkes L. Cerami R. R. Kunz M. Rothschild R. F. Sinta K. Orvek* P. M. Gallagher-Wetmore* V. J. Krukonis*	15th IEEE Lithography Workshop, Kohala Coast, Hawaii, 12-16 August 2002
Quantum-Dot Superlattice Thermoelectric Materials and Devices Research	T. C. Harman P. J. Taylor M. P. Walsh B. E. Laforge	New Thermoelectric Materials Workshop, Traverse City, Michigan, 17-21 August 2002
Fluorocarbon Polymer-Based Photoresists for 157-nm Lithography	T. H. Fedynyshyn W. A. Mowers R. R. Kunz R. E. Sinta M. Sworin A. Cabral J. Curtin	224th ACS Meeting, Boston, Massachusetts, 18-22 August 2002

---

\*Author not at Lincoln Laboratory.

Fluorine—An Enabler in Advanced  
Photolithography

M. Rothschild  
T. M. Bloomstein  
T. H. Fedynyshyn  
V. Liberman  
W. Mowers  
K. Sinta  
M. Switkes  
A. Grenville  
K. Orvek

224th ACS Meeting,  
Boston, Massachusetts,  
18-22 August 2002

Progress in GaN-Based Materials  
and Optical Devices

I. Melngailis

3rd International Conference on  
Advanced Optical Materials  
and Devices,  
Riga, Latvia,  
19-22 August 2002

Superconductive Device  
Fabrication and Development

K. K. Berggren

Quantum Computing Program  
Review,  
Nashville, Tennessee,  
19-23 August 2002

The WIYN One Degree Imager

B. E. Burke  
G. Jacoby\*  
J. Tonry\*  
G. Luppino\*  
C. Claver\*  
B. Starr\*  
A. Saha\*  
C. Harmer\*

Astronomical Telescopes and  
Instrumentation Conference,  
Waikoloa, Hawaii,  
22-28 August 2002

X-Ray Imaging Spectrometer On  
Board Astro-E2

B. E. Burke  
A. Pillsbury

Astronomical Telescopes and  
Instrumentation Conference,  
Waikoloa, Hawaii,  
22-28 August 2002

---

\*Author not at Lincoln Laboratory.

Rubber Focal Plane for Sky Surveys	B. E. Burke J. L. Tonry* G. A. Luppino* N. Kaiser* G. H. Jacoby*	Astronomical Telescopes and Instrumentation Conference, Waikoloa, Hawaii, 22-28 August 2002
Quantum Dot Superlattice Thermoelectric Materials and Devices Research	T. C. Harman P. J. Taylor M. P. Walsh W. D. Goodhue	Diesel Engine Emissions Reduction Technology Conference, San Diego, California, 25 August 2002
Angle Resolved Scattering Measurements of Polished $\text{CaF}_2$ Surfaces and Optical Coatings at 157 nm	T. M. Bloomstein D. E. Hardy M. Rothschild	3rd International Symposium on 157 nm Lithography, Antwerp, Belgium, 3-6 September 2002
Contamination Rates of Optical Surfaces at 157 nm: Impurities Outgassed from Construction Materials and from Photoresists	T. M. Bloomstein J. C. Sedlacek S. T. Palmacci D. E. Hardy V. Liberman M. Rothschild	3rd International Symposium on 157 nm Lithography, Antwerp, Belgium, 3-6 September 2002
Accelerated Laser Induced Damage to $\text{CaF}_2$ and $\text{MgF}_2$ Surfaces	V. Liberman M. Rothschild N. Efremow A. Grenville*	3rd International Symposium on 157 nm Lithography, Antwerp, Belgium, 3-6 September 2002
Long-Term Testing of Optical Coatings for 157-nm Lithography	V. Liberman M. Rothschild N. N. Efremow S. T. Palmacci J. C. Sedlacek A. Grenville*	3rd International Symposium on 157 nm Lithography, Antwerp, Belgium, 3-6 September 2002

---

\*Author not at Lincoln Laboratory.

Immersion Lithography: Optics for  
the 50 nm Mode

M. Switkes  
M. Rothschild

3rd International Symposium  
on 157 nm Lithography,  
Antwerp, Belgium,  
3-6 September 2002

Overview of Optically Pumped  
Mid-IR Lasers Based on Integrated  
Absorber Designs

G. W. Turner  
A. K. Goyal  
M. J. Manfra  
P. J. Foti

5th International Conference on  
Mid-Infrared Optoelectronics  
Materials and Devices,  
Annapolis, Maryland,  
8-11 September 2002

Photonic-Crystal Distributed-  
Feedback Lasers for the Midwave-  
IR

I. Vurgaftman\*  
W. W. Bewley\*  
C. L. Canedy\*  
J. R. Lindle\*  
C. S. Kim\*  
J. R. Meyer\*  
S. J. Spector  
D. M. Lennon  
G. W. Turner  
M. J. Manfra

5th International Conference on  
Mid-Infrared Optoelectronics  
Materials and Devices,  
Annapolis, Maryland,  
8-11 September 2002

Minority Carrier Lifetime in  
*p*-Doped GaInAsSb/GaSb and  
GaInAsSb/AlGaAsSb  
Heterostructures

C. A. Wang  
S. Anikeev\*  
D. Donetsky\*  
G. Belenky\*  
G. Nichols\*

5th International Conference on  
Mid-Infrared Optoelectronics  
Materials and Devices,  
Annapolis, Maryland,  
8-11 September 2002;  
5th Conference on  
Thermophotovoltaic Generation  
of Electricity,  
Rome, Italy,  
15-19 September 2002

Non-Contact Determination of Free  
Carrier Concentration in *n*-Type  
GaSb and GaInAsSb

C. A. Wang  
J. E. Maslar\*  
W. S. Hurst\*

5th International Conference on  
Mid-Infrared Optoelectronics  
Materials and Devices,  
Annapolis, Maryland,  
8-11 September 2002

---

\*Author not at Lincoln Laboratory.



Wafer-Bonded Internal Reflectors  
for Enhanced TPV Performance

C. A. Wang  
P. G. Murphy  
P. W. O'Brien  
D. A. Shiau  
A. C. Anderson

5th Conference on  
Thermophotovoltaic Generation  
of Electricity,  
Rome, Italy,  
15-19 September 2002

Lattice-Matched GaInAsSb/  
AlGaAsSb/GaSb  
Thermophotovoltaic Devices

C. A. Wang  
C. J. Vineis  
R. H. Huang  
M. K. Connors  
H. K. Choj\*  
L. R. Danielson\*  
G. Nichols\*  
D. Donetsky\*  
S. Anikeev\*  
G. Belenky\*

5th Conference on  
Thermophotovoltaic Generation  
of Electricity,  
Rome, Italy,  
15-19 September 2002

Inherently Planar Fully Depleted  
SOI Isolation

J. A. Burns  
C. Costa  
K. Warner

28th Annual IEEE International  
SOI Conference,  
Williamsburg, Virginia,  
7-10 October 2002

3D Mode Converters for SOI  
Integrated Optics

M. Fritze  
J. Fijol\*  
S. Jacobson\*  
P. Keating\*  
C. Manolatu\*  
J. Knecht  
C. Bozler  
J. LeBlanc\*  
E. Fike\*  
B. Kessler\*  
C. Keast  
M. Frish\*

28th Annual IEEE International  
SOI Conference,  
Williamsburg, Virginia,  
7-10 October 2002

---

\*Author not at Lincoln Laboratory.

Low Temperature Oxide Bonded  
Three-Dimensional Integrated  
Circuits

K. Warner  
W. Mowers  
J. A. Burns  
D. Lennon  
C. L. Keast  
D. R. Yost  
A. Loomis  
R. Kunz

28th Annual IEEE International  
SOI Conference,  
Williamsburg, Virginia,  
7-10 October 2002

Slab-Coupled Semiconductor  
Lasers with Single-Spatial, Large-  
Diameter Mode

J. P. Donnelly  
R. K. Huang  
J. N. Walpole  
L. J. Missaggia  
C. T. Harris

Quantum Electronics and  
Optics Seminar,  
Massachusetts Institute of  
Technology,  
Cambridge, Massachusetts,  
23 October 2002

CANARY B-Cell Sensor for Rapid  
Identification of Pathogens

M. S. Petrovick

Council of Security and  
Strategic Technology  
Organizations (COSTO)  
Conference,  
Arlington, Virginia,  
14-17 October 2002

Three-Dimensional Imaging Using  
Geiger-Mode Avalanche  
Photodiode Arrays

B. F. Aull

Lincoln Laboratory  
Technical Seminar Series,  
Yale University,  
New Haven, Connecticut,  
30 October 2002

CANARY B-Cell Sensor for Rapid  
Identification of Pathogens

M. A. Hollis

Lincoln Laboratory  
Technical Seminar Series,  
Old Dominion University,  
Norfolk, Virginia,  
31 October 2002

This Page Intentionally  
Left Blank

## ORGANIZATION

### SOLID STATE DIVISION

D. C. Shaver, Head  
R. W. Ralston, Associate Head  
N. L. DeMeo, Jr., Assistant  
Z. J. Lemnios, Senior Staff  
K. J. Challberg, Administrative Staff  
J. D. Pendergast, Administrative Staff

#### SUBMICROMETER TECHNOLOGY

M. Rothschild, Leader  
T. M. Lysczarz, Assistant Leader  
T. H. Fedynyshyn, Senior Staff  
R. R. Kunz, Senior Staff

Astolfi, D. K.	Lennon, D. M.
Bloomstein, T. M.	Liberman, V.
Cann, S. G.	Palmacci, S. T.
Creel, C. R.	Pottebaum, I. S.
DiNatale, W. F.	Sedlacek, J. H. C.
Efremow, N. N., Jr.	Spector, S. J.
Geis, M. W.	Stallman, J. B.
Goodman, R. B.	Switkes, M.
Krohn, K. E.	Sworin, M.
Leibowitz, F. L.	Yoon, J. U.

#### QUANTUM ELECTRONICS

A. Sanchez-Rubio, Leader  
T. Y. Fan, Assistant Leader  
T. H. Jeys, Senior Staff  
J. J. Zayhowski, Senior Staff

Aggarwal, R. L.	Herzog, W. D.
Augst, S. J.	Hybl, J. D.
Daneu, J. L.	Lynch, E. J.
Daneu, V.	O'Brien, P. W.
Desmarais, L.	Ochoa, J. R.
Goyal, A. K.	Ripin, D. J.

#### ELECTRO-OPTICAL MATERIALS AND DEVICES

J. C. Twichell, Leader  
G. W. Turner, Assistant Leader  
D. L. Spears, Senior Staff  
C. A. Wang, Senior Staff  
R. C. Williamson, Senior Staff

Bailey, R. J.	Huang, R. K.	Mull, D. E.
Calawa, D. R.	Juodawlkis, P. W.	Napoleone, A.
Calawa, S. D.	LaForge, B. E.	Nitishin, P. M.
Connors, M. K.	Liau, Z. L.	Oakley, D. C.
Donnelly, J. P.	Mahoney, L. J.	O'Donnell, F. J.
Goodhue, W. D.	Manfra, M. J.	Plant, J. J.
Groves, S. H.	McIntosh, K. A.	Shiau, D. A.
Hargreaves, J. J.	Missaggia, L. J.	Taylor, P. J.
Harman, T. C.	Molnar, R. J.	Younger, R. D.
Harris, C. T.		

BIOSENSOR AND MOLECULAR  
TECHNOLOGIES

M. A. Hollis, Leader  
T. H. Rider, Senior Staff

Blanchard, D. J.	Nargi, F. E.
Cabrera, C. R.	Parameswaran, L.
Graves, C. A.	Petrovick, M. S.
Harper, J. D.	Postema-Zook, C. E.
Lakdawala, S.	Schmidt, T. L.
Mathews, R. H.	Schwoebel, E. D.

ANALOG DEVICE TECHNOLOGY

M. A. Gouker, Leader  
L. M. Johnson, Assistant Leader  
A. C. Anderson, Senior Staff

Berggren, K. K.	Oates, D. E.
Boisvert, R. R.	Sage, J. P.
Fitch, G. L.	Santiago, D. D.
Lyons, W. G.	Seaver, M. M.
Macedo, E. M., Jr.	Slattery, R. L.
Murphy, P. G.	Weir, T. J.

ADVANCED IMAGING TECHNOLOGY

B. B. Kosicki, Leader  
R. K. Reich, Assistant Leader  
B. E. Burke, Senior Staff

Aull, B. F.	Loomis, A. H.
Ciampi, J. S.	Mallen, R. D.
Cooper, M. J.	McGonagle, W. H.
Craig, D. M.	O'Mara, D. M.
Daniels, P. J.	Osgood, R. M.
Doherty, C. L., Jr.	Percival, K. A.
Dolat, V. S.	Rathman, D. D.
Felton, B. J.	Rose, M. K.
Gregory, J. A.	Stern, A.
Johnson, K. F.	Young, D. J.
Lind, T. A.	

ADVANCED SILICON TECHNOLOGY

C. L. Keast, Leader  
V. Suntharalingam, Assistant Leader  
P. W. Wyatt, Senior Staff

Austin, E. E.	Lui, N. S.
Berger, R.	Muldavin, J. B.
Bozler, C. O.	Newcomb, K. L.
Brunelle, M. R.	Rabe, S.
Burns, J. A.	Soares, A. M.
Chen, C. K.	Travis, L.
Chen, C. L.	Tyrrell, B. M.
D'Onofrio, R. P.	Warner, K.
Fritze, M.	Wheeler, B. D.
Gouker, P. M.	Yost, D.-R.
Healey, R. E.	Young, G. R.
Knecht, J. M.	

# 1. QUANTUM ELECTRONICS

## 1.1 LASER-INDUCED BREAKDOWN SPECTROSCOPY FOR THE DETECTION AND CLASSIFICATION OF BIOLOGICAL AEROSOLS

Methods for the accurate characterization of ambient biological aerosols are required for detecting biological warfare agents, monitoring indoor air quality, and preventing the spread of airborne infectious diseases in health care facilities. Current sensor technologies determine either the total aerosol concentration or the total *biological* aerosol concentration by measuring the intrinsic fluorescence [1] of aerosol particles. Actual identification of bioaerosols is usually accomplished by slower and more expensive antibody, culture, or DNA based techniques. Technologies that offer improved discrimination between classes of bioaerosols would substantially reduce the deployment cost of bioaerosol detection systems and allow optical sensors to operate independently in certain limited-role applications.

Elemental analysis would provide a set of information orthogonal and complementary to fluorescence for the detection and classification of bioaerosols. Biological organisms contain a wide variety of inorganic elements such as Ca, Mg, Mn, Fe, P, Na, K, and Si [2]; this suggests high potential for atomic spectroscopy as a bioaerosol classifier. Laser-induced breakdown spectroscopy (LIBS) is one technique for bringing atomic spectroscopy to the field. Elemental spectra are acquired by using a tightly focused laser pulse to generate a short-lived plasma that vaporizes, atomizes, and thermally excites the sample (in this case an aerosol particle). Atomic emission lines from the hot plasma are then recorded with a spectrometer and array detector. The experimental simplicity, the portability of modern lasers, and the lack of required sample preparation make LIBS an attractive and practical technique for deployment into field instruments.

To ascertain the potential of LIBS as a bioaerosol sensor, spectra of bulk materials representative of ambient biological aerosols were recorded. These included three types of sporulated *Bacillus globigii* (Bg) that differed in growth history and/or preparation; three "media" representing viruses, toxins, and growth media; three types of mold spores; and three types of pollen. Spectra of three varieties of dirt were also included to represent common nonbiological aerosols. A 50-mJ, 7-ns, 1064-nm laser pulse was used to generate a plasma. Atomic emission lines were detected by two time-gated Ocean Optics HR2000 spectrometers that covered the wavelength range 200–825 nm. The various samples were aerosolized into a thick cloud for LIBS measurement. Therefore, spectra from a single laser shot resulted from multiple aerosol particles. The resulting spectra were used to identify the spectral lines containing the most useful information for discriminating against backgrounds (mold and pollen) and for classifying the bioaerosols (Bg and media). In order to illustrate the discrimination capability in the laser-induced breakdown spectra, principal component analysis was applied to the 25 most prominent lines in the spectra.

Figure 1-1 shows representative single-shot spectra of the four classes of material, with a few common elemental lines identified. Visual inspection of these spectra indicates good separability. For

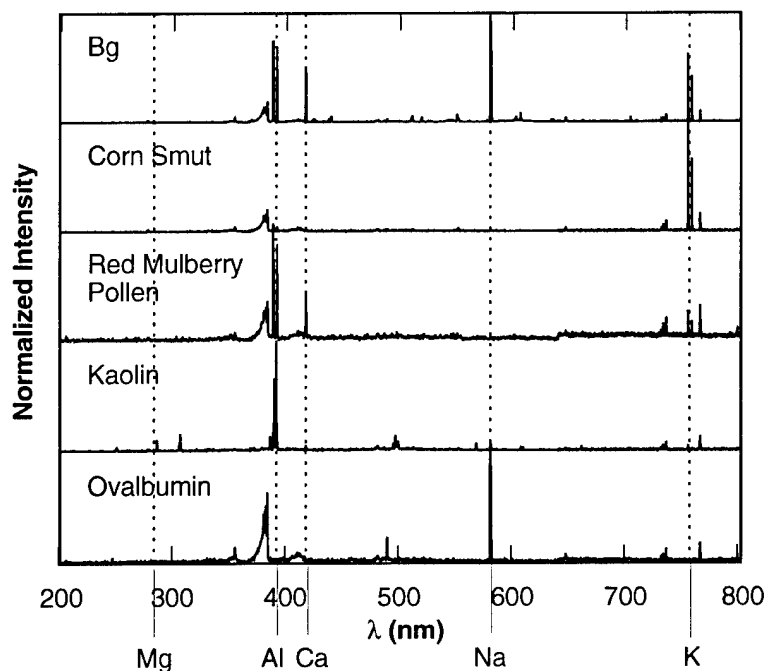


Figure 1-1. Representative single-shot laser-induced breakdown spectra of aerosolized samples. Although the spectra are taken from a single shot and charge-coupled device exposure, the aerosol cloud was sufficiently concentrated that multiple particles contribute to each spectrum.

example, the ratio of K:Ca provides good discrimination between Bg and corn smut and a Na:Ca ratio separates red mulberry pollen from Bg. Figure 1-2 shows the results of a principal components analysis (PCA) of the four classes of bioaerosols. To find the principal components that best separate the populations, a training set was constructed from average spectra of each bioaerosol class. Once the PCA components were determined, the entire data set was transformed into the PCA coordinate system to generate the three-dimensional scatter plot. In this case the first three principal components represent >95% of the training set's variance (or information content). As illustrated in Figure 1-2, LIBS does a remarkably good job of separating the different bioaerosols even in the presence of different types of Bg, mold, pollen, and media. Pollen seems to have the most variability, some of this likely resulting from the low signal to noise of the pollen LIBS spectra relative to the other samples.

Figure 1-3 shows the results of applying PCA within the various bioaerosol classes. In these cases, training sets were constructed using average spectra of each sample type. The scatter plots indicate that LIBS also has significant capability for separating Bg types according to growth history and preparation method, and for distinguishing between the different media and mold spores. This capability could be valuable for recording "fingerprints" of specific bioagents.

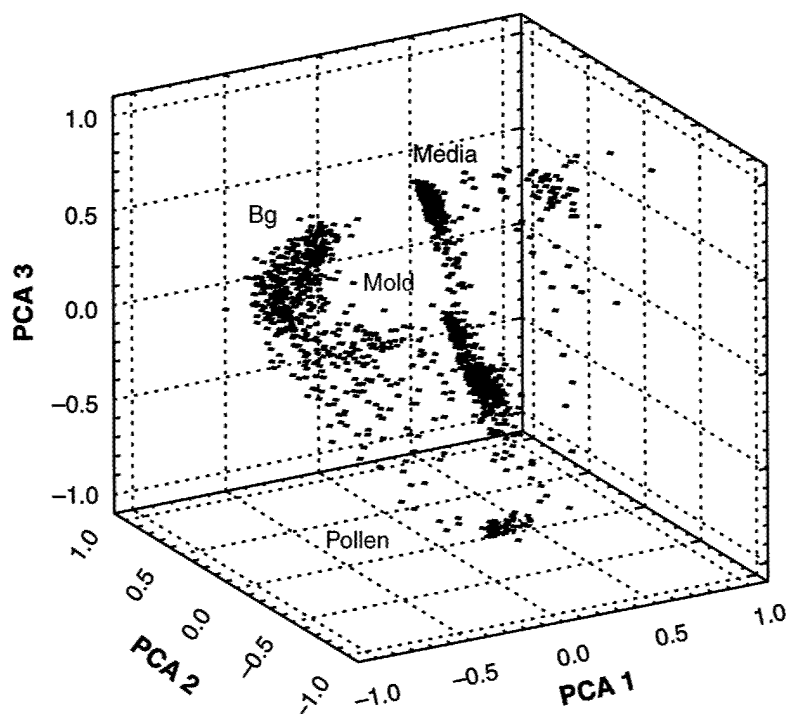


Figure 1-2. Three-dimensional scatter plot of entire data set in the principal component analysis (PCA) coordinates. Each plot symbol represents a single spectrum acquired from a single laser shot. The principal components were computed using three linear combinations of the intensities of 29 lines from the spectra. Each class of bioaerosol contains three different types, e.g., the mold category is composed of penicillium, corn smut, and oat smut.

These initial results show that LIBS is promising as a classifier and high-discrimination bioaerosol sensing technique. They also suggest that LIBS may have considerable utility in differentiating between bioaerosols of the same species but different origins. Consideration of the mass composition of bioaerosols and LIBS signal strength indicates that single-particle LIBS of single bioaerosols is feasible. Combination of single-particle LIBS with current fluorescence sensing technology should lead to a high-discrimination bioaerosol classifier operating with the throughput and sensitivity needed for real-world applications.

J. D. Hybl

#### REFERENCES

1. S. Hill, R. Pinnick, S. Niles, Y. Pan, S. Holler, R. Chang, J. Bottiger, B. Chen, C. Orr, and G. Feather, *Field Anal. Chem.* 3 (4-5), 221 (1999).
2. G. Gould and A. Hurst, *The Bacterial Spore* (Academic, London, 1969).



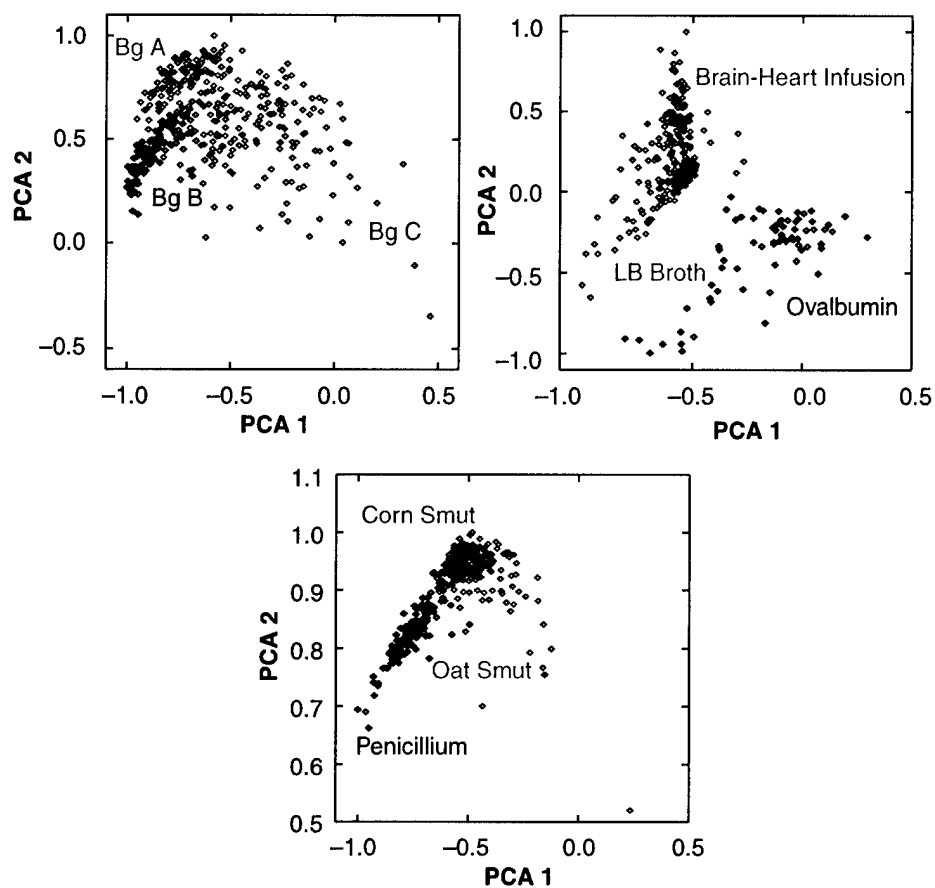


*Figure 1-3. PCA plots of each bioaerosol class where the principal components were determined from training sets comprising average spectra of each specific type of bioaerosol. In all three cases the first two principal components account for >95% of the training set's variance.*

## 2. ELECTRO-OPTICAL MATERIALS AND DEVICES

### 2.1 WAFER-BONDED INTERNAL BACK-SURFACE REFLECTORS FOR ENHANCED GaInAsSb/GaSb TPV PERFORMANCE

High-efficiency thermophotovoltaic (TPV) systems require highly efficient TPV cells as well as excellent spectral control to recuperate below-band-gap photons back to the radiator [1]. A back-surface reflector (BSR), which is a highly reflecting mirror deposited on the back side of the substrate, was used to provide both spectral control and device performance enhancement for InGaAs/InP TPV devices [2],[3]. Spectral control is achieved by reflection of below-band-gap photons that pass through the device and substrate back to the radiator, while device improvement results from the increased probability of above-band-gap photons that are not absorbed in the first pass to be reflected back into the active layers for a second-pass absorption. This approach, however, has not been pursued for GaSb-based TPV systems since the effectiveness of the BSR is reduced by free-carrier absorption in the GaSb substrate [4].

Here, we describe a new approach for GaInAsSb/GaSb TPV cells with an internal BSR, which in effect eliminates problems associated with substrate absorption. The GaInAsSb/GaSb epitaxial layers are wafer bonded to a GaAs handle wafer with a dielectric/Au reflector. This concept of wafer bonding using metal as an adhesive layer is similar to that developed for integration of dissimilar materials [5] and for fabrication of internal mirrors for photovoltaic cells [6], light-emitting diodes [7], and vertical-cavity surface-emitting lasers [8]. The resulting GaInAsSb/GaSb TPV device structure consists of a broadband high-reflectivity dielectric/Au mirror sandwiched between the device layers and the GaAs handle substrate. This configuration has the potential for not only improving TPV cell performance and providing spectral control, but also for monolithically interconnecting TPV cells in series. Specifically, the internal BSR enhances photon-recycling effects, and increases the effective optical thickness so that the active layers can be thinner, which is advantageous for reducing dark current and increasing open-circuit voltage. In addition, reflection of below-band-gap photons back to the radiator can aid in spectral control. Furthermore, since the epitaxial layers are electrically isolated from the handle substrate by the dielectric layer, TPV cells can be connected in series to fabricate monolithically interconnected modules (MIMs) [2],[3].

GaInAsSb/GaSb TPV device structures were grown lattice matched to 5-cm-diam GaSb substrates by organometallic vapor-phase epitaxy [9]. Epitaxial layers were grown in a reverse sequence compared to conventional TPV structures in order to obtain a *p*-on-*n* structure after wafer bonding. In addition, an InAsSb layer was grown as the etch-stop layer. The as-grown inverted TPV structure shown in Figure 2-1(a) consists of the following layers grown on a (001) *n*-GaSb substrate miscut 6° toward (1-11)B: *u*-GaSb buffer layer, *u*-InAsSb etch-stop layer, *p*-GaSb contact layer, *p*-AlGaAsSb window layer, *p*-GaInAsSb emitter layer, *n*-GaInAsSb base layer, and *n*-GaSb lateral conduction layer (LCL). (In some structures, the *p*-AlGaAsSb window layer was omitted.) Although the InAsSb etch-stop layer is eventually removed during fabrication of wafer-bonded epitaxial TPV structures, it is critical that this layer is also lattice matched to GaSb since the GaInAsSb active layers are grown on top of the InAsSb etch-stop layer.

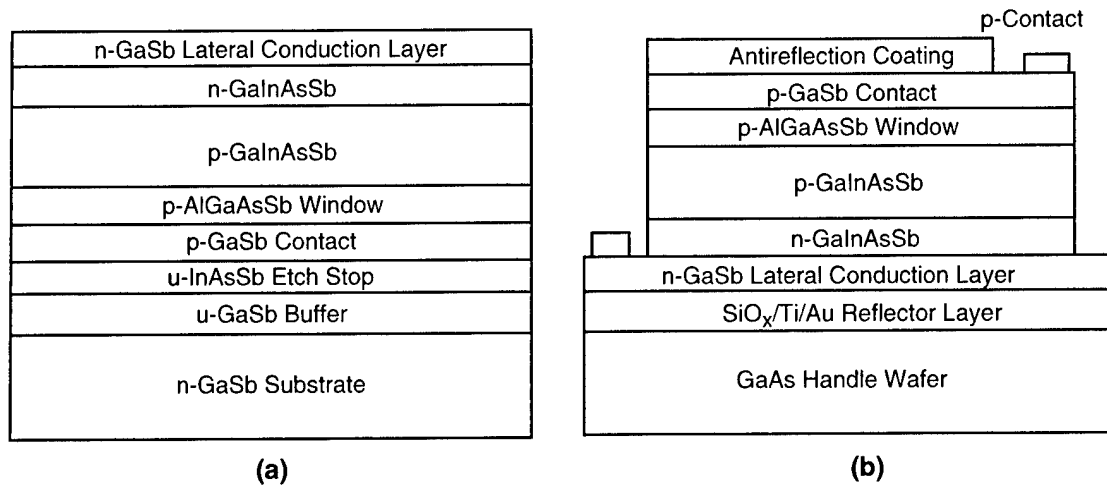


Figure 2-1. Schematic structure of (a) inverted GaInAsSb/GaSb thermophotovoltaic (TPV) device structure grown on n-GaSb substrate for wafer bonding, and (b) wafer-bonded GaInAsSb/GaSb TPV structure on GaAs handle wafer after removal of GaSb substrate and InAsSb etch-stop layer.

The inverted TPV structure on the GaSb substrate and the handle semi-insulating GaAs wafer were prepared for bonding with a dielectric/reflector. First, both GaSb and GaAs surfaces were solvent cleaned and etched in HCl and NH<sub>4</sub>OH to remove native oxides. The GaSb epitaxial TPV structure was sputter coated with a three-layer reflector consisting of SiO<sub>x</sub>/Ti/Au, while the GaAs was sputter coated with Ti/Au. SiO<sub>x</sub> not only provides electrical isolation of the epitaxial layers but also increases above-band-gap reflectivity. Although Ti decreases the reflectivity, it improves the adhesion of Au to both the SiO<sub>x</sub> and GaAs. To bond the wafers, the two Au surfaces were placed in contact, and the wafers were heated under vacuum to a temperature of 250°C, and a mechanical pressure of 250 psi was applied. The low bonding temperature is compatible with subsequent wafer processing. In a separate set of experiments to study reflector properties, GaAs wafers were sputter coated with SiO<sub>x</sub> of various thicknesses ranging from 500 to 3600 nm and a 0.5-μm-thick Au layer.

The 5-cm-diam bonded wafer was cut into four quarters for ease of handling and processing, and the GaSb substrate was spin etched with H<sub>2</sub>O<sub>2</sub>:H<sub>2</sub>O:NaK tartrate tetrahydrate to remove the bulk of the substrate, and then chemomechanically polished. The remaining GaSb substrate and GaSb buffer layer were selectively etched using CrO<sub>3</sub>:HF:H<sub>2</sub>O until the InAsSb layer was exposed. Finally, the InAsSb etch-stop layer was removed with H<sub>2</sub>O<sub>2</sub> saturated with citric acid. The resulting wafer-bonded epitaxy can then be processed into TPV devices using standard photolithographic processes and chemical etching to define the TPV cells. Figure 2-1(b) schematically shows the wafer-bonded GaInAsSb/GaSb TPV device structure with the internal BSR.

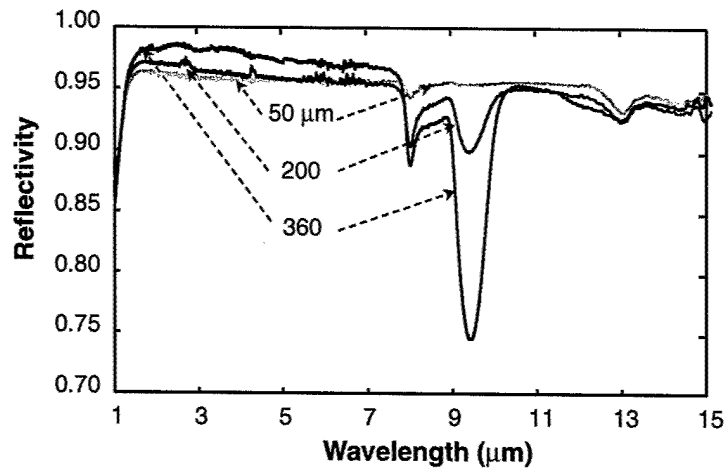


Figure 2-2. Measured reflectivity of  $\text{SiO}_x/\text{Au}$  reflector with various  $\text{SiO}_x$  thicknesses on GaAs.

Figure 2-2 shows the measured reflectivity of the  $\text{SiO}_x/\text{Au}$  reflector, with various  $\text{SiO}_x$  thicknesses of 50, 200, and 360 nm, as measured through the GaAs wafer. For wavelengths below  $\sim 5 \mu\text{m}$ , the reflectivity increases with thickness. Above  $5 \mu\text{m}$ , absorption in  $\text{SiO}_x$  decreases the reflectivity, especially in the wavelength range between  $7.5$  and  $10 \mu\text{m}$ . Below  $1.4 \mu\text{m}$ , the reflectivity decreases because of absorption in the GaAs substrate. High reflectivity below  $2.5 \mu\text{m}$  is important for enhancing GaInAsSb TPV device performance, while above  $2.5 \mu\text{m}$  it is important for spectral control. The integrated reflectivity from  $1.5$  to  $2.5 \mu\text{m}$  (since GaAs is absorbing below  $1.4 \mu\text{m}$ ) is  $0.962$ ,  $0.97$ , and  $0.981$  for  $\text{SiO}_x$  thickness of  $50$ ,  $200$ , and  $360$  nm, respectively. For  $2.5$ – $15 \mu\text{m}$ , the integrated reflectivity is  $0.952$ ,  $0.943$ , and  $0.936$  for  $\text{SiO}_x$  thickness of  $50$ ,  $200$ , and  $360$  nm, respectively. The high reflectivity over the wide wavelength range is extremely attractive for GaSb-based TPV systems, although a trade-off exists between above- and below-band-gap reflector performances when using  $\text{SiO}_x$ . Further improvements in reflective properties of the internal BSR are expected by replacement of  $\text{SiO}_x$  with an alternative low-index dielectric with low absorption above  $2.5 \mu\text{m}$ , such as  $\text{MgF}_2$ ,  $\text{AlF}_3$ , or other metal fluorides [10]. As a starting point in this study, the  $\text{SiO}_x$  thickness of the BSR layer used for wafer-bonded samples was  $200$  nm. In these structures, Ti was deposited on the  $\text{SiO}_x$  to improve Au adhesion, and the reflectivity decreased by only a few percent.

Interferograms of the GaInAsSb/GaSb and GaAs bonded wafers are shown in Figure 2-3. The GaSb wafer is concave and exhibits an average wafer bow of  $22 \mu\text{m}$ , while the GaAs is convex with a bow of  $24 \mu\text{m}$ . The circular fringes and nearly symmetrical wafer bow are indicative that bonding of the TPV device wafer and GaAs wafer was achieved over the entire  $5$ -cm-diam area. The bow is due to residual stress in the bonded wafers, and it results from different thermal expansion coefficients of the  $\text{SiO}_x$ , Au, GaSb, and GaAs alloys. If this residual stress exceeds the mechanical bond strength of the sputtered and bonded layers, debonding can occur. Furthermore, adhesion of the sputtered layers and the bonded interface must

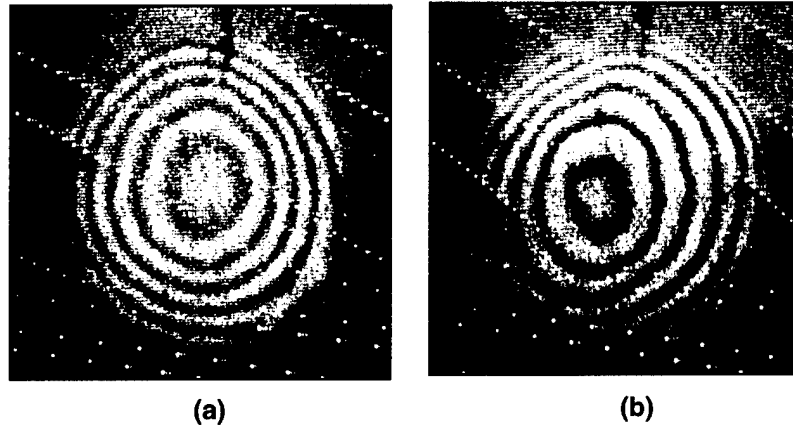


Figure 2-3. Interferograms of (a) back side of GaSb substrate bonded to GaAs handle substrate, and (b) back side of GaAs handle substrate. One fringe corresponds to  $4.8\ \mu\text{m}$ .

be able to withstand substrate removal and multiple processes during TPV fabrication. In numerous tests, the integrity of the Au-bonded epitaxial layers was maintained throughout all processing steps.

The high-resolution x-ray diffraction rocking curves for the lattice-matched control GaInAsSb TPV device structure on a GaSb substrate and for a wafer-bonded GaInAsSb TPV structure after removal of the GaSb substrate and InAsSb etch-stop layer are shown in Figures 2-4(a) and 2-4(b), respectively. The diffraction intensity is lower for the wafer-bonded TPV device structure since the GaSb substrate has been removed and only the epitaxial layers that were grown lattice matched to GaSb are remaining. The slightly broadened peak of the wafer-bonded structure is due to residual stress.

Figure 2-5 shows 300-K photoluminescence (PL) spectra for the control and wafer-bonded GaInAsSb TPV structures. Multiple peaks in the PL spectrum of the wafer-bonded sample are due to thin-layer interference effects discussed below. The PL peak intensity of the wafer-bonded epitaxy is over two times greater than that of the control TPV structure. These results suggest that the optical efficiency is enhanced as a result of the internal BSR, and there is negligible material degradation after wafer bonding and substrate removal.

Figure 2-6 shows the reflectivity of the wafer-bonded GaInAsSb TPV device structure with and without an antireflection (AR) coating. Without the AR coating, resonant absorption is observed across the whole wavelength range because of destructive interference between reflections from the air/GaSb ( $R \sim 34\%$ ) and GaSb/SiO<sub>x</sub>/Ti/Au interfaces. Such effects introduce absorption losses and will reduce the efficiency of the internal BSR [11]. Other approaches, however, could minimize these effects. One is to utilize an AR coating on the front surface of the TPV cell to minimize resonant absorption of above-band-gap photons, as shown in Figure 2-6, and another is to use a thinner TPV device layer structure, which increases the fringe spacing.

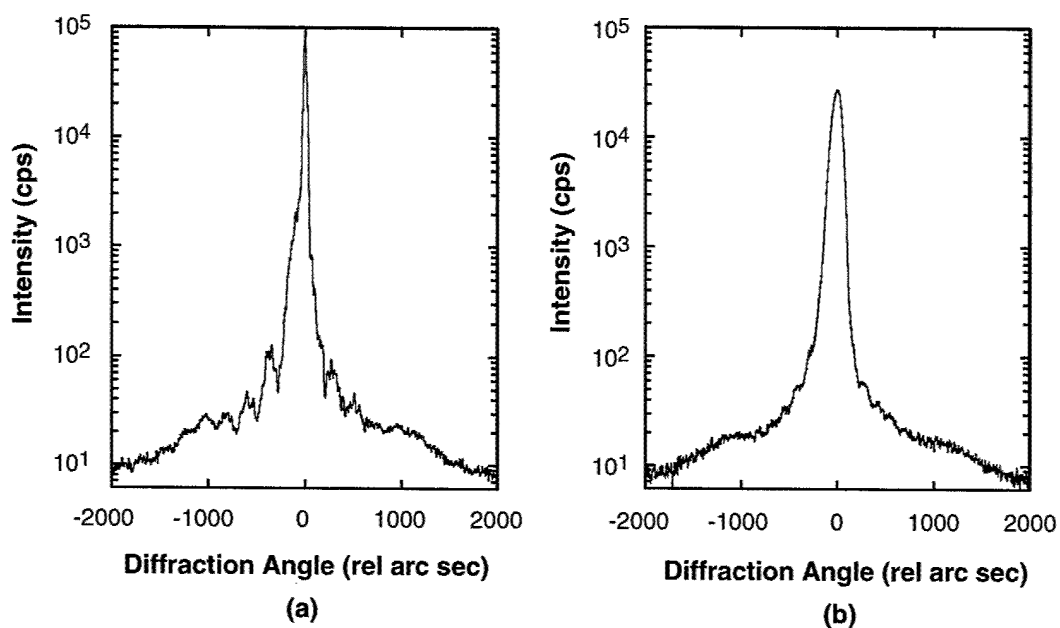


Figure 2-4. X-ray diffraction of (a) control GaInAsSb/GaSb TPV wafer and (b) wafer-bonded GaInAsSb/GaSb TPV structure.

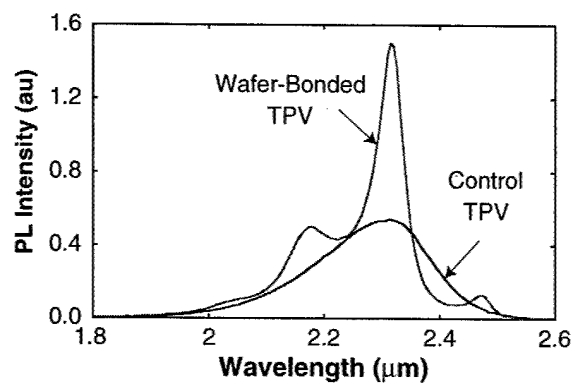


Figure 2-5. 300-K photoluminescence of control and wafer-bonded GaInAsSb/GaSb TPV structures.

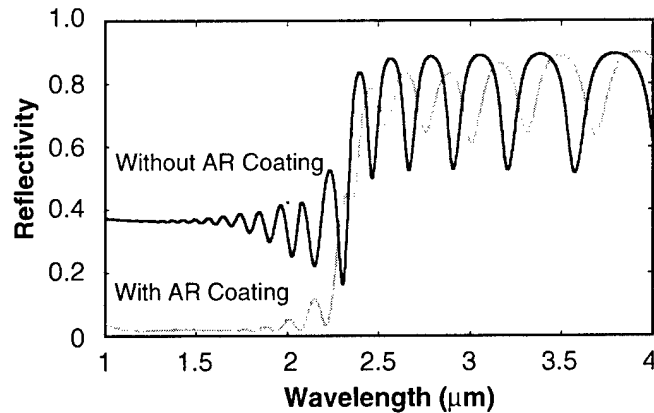


Figure 2-6. Reflectivity spectrum of uncoated and antireflection-coated wafer-bonded GaInAsSb/GaSb TPV structure. The TPV device structure is 4  $\mu\text{m}$  thick. Thinner device layers will increase the resonant fringe spacing.

In summary, wafer bonding of epitaxial GaInAsSb/GaSb TPV device layers to GaAs substrates with a high-reflectivity broadband mirror was achieved. The structural and optical properties of the wafer-bonded TPV device layers were maintained after fabrication. Since the BSR provides electrical isolation of the TPV device layers, GaInAsSb TPV devices could be monolithically interconnected. These results indicate that this approach is extremely attractive for GaSb-based TPVs fabricated with MIM architecture. The wafer-bonding process is not limited to GaAs substrates, and alternative handle substrates can also be considered.

C. A. Wang	P. G. Murphy
P. W. O'Brien	D. A. Shiau
A. C. Anderson	D. M. DePoy*
G. Nichols*	

## 2.2 GEIGER-MODE InGaAsP/InP AVALANCHE PHOTODIODES FOR PHOTON COUNTING AT 1.06 $\mu\text{m}$

Geiger-mode avalanche photodiodes (APDs), which can generate milliamp-level current pulses and logic compatible voltage swings in response to single absorbed photons, are useful for passive or

---

\*Author not at Lincoln Laboratory.

active sensing applications with few available photons. Silicon photon-counting APDs, however, are typically limited to <20% quantum efficiency (QE) and <2% photon detection efficiency at 1.06  $\mu\text{m}$  [12]. Here, we describe the development of InGaAsP/InP Geiger-mode APDs designed for sensitive photon-counting performance at 1.06  $\mu\text{m}$ . Many groups have investigated InGaAs/InP APDs during the past 15 years for photon-counting applications at 1.3–1.5- $\mu\text{m}$  wavelengths, but little optimization has been reported for 1.06- $\mu\text{m}$  wavelengths. In addition to optimization of performance at 1.06  $\mu\text{m}$ , a primary goal of this effort is the development of small arrays ( $4 \times 4$  and  $32 \times 32$ ) of Geiger-mode APDs for insertion as focal planes in three-dimensional imaging laser radar (Ladar) systems.

The APDs are mesa-isolated separate absorber multiplier (SAM) structures with a field-stop design, as shown in Figure 2-7. Early measurements indicated the primary sources of dark current at breakdown were generation current in the InGaAsP absorber and tunneling current (through defects) in the InP avalanche region. Generation current decreases with temperature, essentially as the intrinsic carrier concentration, while tunneling in the avalanche region is weakly dependent on temperature. Therefore, tunneling eventually becomes the major source of dark current as the temperature is reduced, even if it is not dominant at 300 K. Since tunneling depends exponentially on the inverse of the electric field, field-stop designs, which have a lower peak field in the avalanche region than designs without a field stop, have lower tunneling current at breakdown. Defect-assisted tunneling current in the avalanche region is reduced to acceptable levels ( $<10^{-8} \text{ A/cm}^2$ ) in APD designs with  $\sim 0.8\text{-}\mu\text{m}$  avalanche region width (maximum field  $<5 \times 10^5 \text{ V/cm}$ ). To minimize tunneling in the absorber, the maximum field in the absorber is required to be  $\leq 2 \times 10^5 \text{ V/cm}$ . For use at 300 K, this places a lower limit on the integrated charge in the field stop. The absorber should also remain fully depleted at the reduced voltage needed to reach breakdown at reduced operating temperatures. This places an upper limit on the field-stop charge.

Detector materials were grown by organometallic vapor-phase epitaxy in an atmospheric pressure chimney-geometry reactor with susceptor rotation. Epitaxial layers were grown lattice matched to Zn-doped (mid- $10^{18} \text{ cm}^{-3}$ ) InP substrates. Photoluminescence measurements indicate a peak position in the range  $1200 \pm 6 \text{ nm}$  for the quaternary absorber layers, and X-ray diffraction measurements show that lattice mismatch between the InGaAsP and the InP substrate is  $<5 \times 10^{-4}$ .

Mesa devices were fabricated using a  $\text{SiO}_2$  etch mask and wet chemical etching. The sidewalls of the mesa were passivated with polyimide, and Ti/Au top contacts were aligned to a via in the polyimide. Back contact was made to the InP substrate. Front-illuminated arrays of APDs were fabricated with the diameter of detectors varied from 32 to 60  $\mu\text{m}$  on a 100- $\mu\text{m}$  pitch. Also shown in Figure 2-7 are scanning electron micrographs of a single detector and  $4 \times 4$  array, which includes pads for wire bonding electrical connections to external bias/timing circuitry.

Current-voltage (I-V) measurements indicate that dark current density in fully depleted devices at room temperature ranges from  $2 \times 10^{-8}$  to  $5 \times 10^{-7} \text{ A/cm}^2$ , depending on growth and design parameters. This current density is consistent with generation current in the InGaAsP absorber if the effective lifetimes are  $\sim 0.1\text{--}2 \text{ }\mu\text{s}$ . Carrier lifetimes in the microsecond range are an indication of excellent material quality with few defects. By rastering focused 1.06- $\mu\text{m}$ -wavelength light from a cw Nd:YAG laser across a



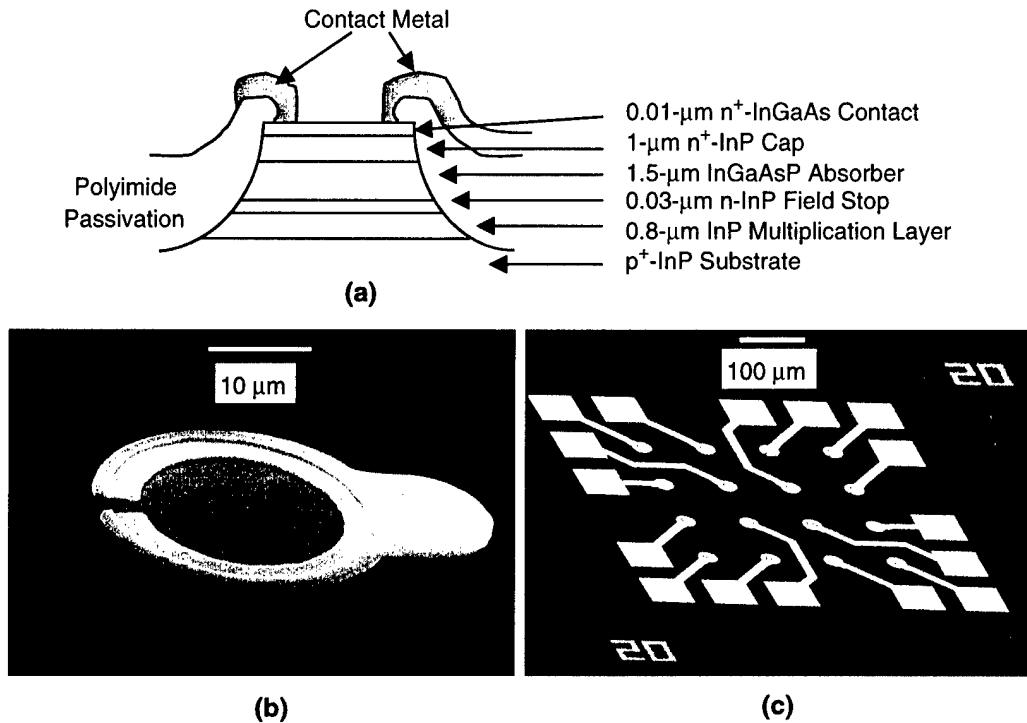


Figure 2-7. (a) Drawing of layer design and mesa structure of avalanche photodiode (APD), and micrographs showing (b) single detector and (c)  $4 \times 4$  detector array.

detector when it is biased in linear gain mode, the uniformity of optical response and an accurate value for the QE were measured. Less than 10% variation in response across the detectors is typically found at a gain of 20. Unity gain external QE is found to be  $\sim 55\%$ , in reasonable agreement with expected values for uncoated devices with a  $1.5\text{-}\mu\text{m}$ -thick absorber layer.

The important figures of merit for determining the sensitivity of a Geiger-mode APD are the dark count rate (DCR) and photon detection efficiency (PDE). To measure these parameters, detectors are biased slightly below breakdown and then gated above breakdown for a short time, typically  $\sim 1\text{ }\mu\text{s}$ , at a repetition frequency of  $\sim 5\text{ kHz}$ . The magnitude of the applied voltage above breakdown is referred to as the overbias. The length of time a device remains biased above breakdown before an avalanche occurs without illumination is Poisson distributed, with a characteristic hold-off time  $\tau_{\text{HO}}$ , where  $\text{DCR} = 1/\tau_{\text{HO}}$ . The PDE is measured in a similar fashion, with continuous  $1.064\text{-}\mu\text{m}$  illumination at picowatt power levels focused on the active area of the detector. The DCR is factored out in determining the measured PDE values. Thousands of gate periods are averaged for each measured value of DCR and PDE. Shown in Figure 2-8 are the DCR and PDE measured for representative  $33\text{-}\mu\text{m}$ -diam detectors from two wafers at

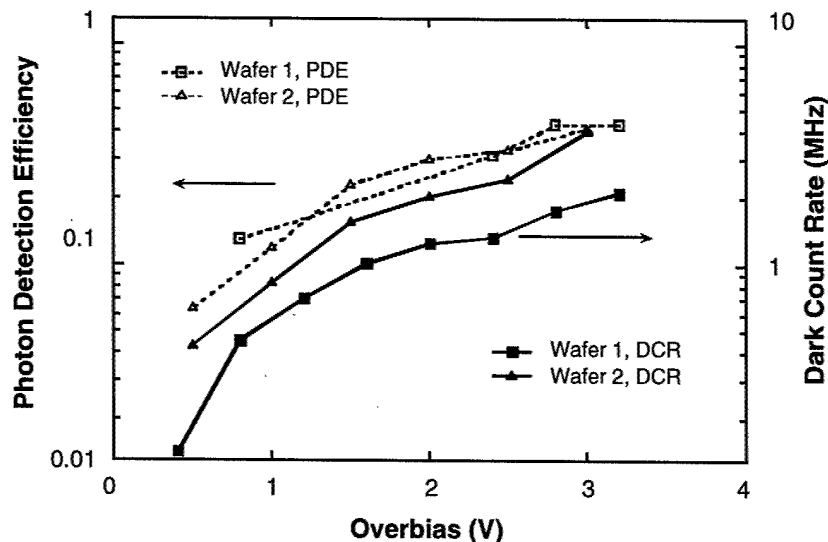


Figure 2-8. Overbias dependence of photon detection efficiency and dark count rate in 33- $\mu$ m-diam detectors from wafer 1 and wafer 2 at room temperature.

room temperature as a function of the overbias in the device. With 2.8 V of overbias, 33% PDE and 1.7-MHz DCR are measured for the wafer 1 device. Wafer 2 shows almost identical PDE, although the DCR is higher than for wafer 1, as expected because of higher generation current in this sample.

When an APD is biased above breakdown, the device has some probability of undergoing a Geiger avalanche event. As overbias is increased, the measured DCR and PDE increase in a similar fashion up to 2.5–3 V of overbias, indicative of the increasing breakdown probability  $P_{BD}$ . A 33% PDE represents a 60% probability of counting each primary photocarrier generated in the detector, since  $PDE = QE \cdot P_{BD}$ . Assuming the same 60% probability of being counted, the 1.7-MHz DCR for the wafer 1 detector corresponds to a multiplied primary dark current of 280 fA, in close agreement with primary dark current density measured on large test diodes. Although greater overbias increases the avalanche probability, the DCR will increase faster because additional tunneling-related current is created in the InP. Thus, the optimum overbias is found near 3 V. The DCR was found to scale with the area of the detector, indicating little contribution from generation at the mesa edges.

Reduction in the DCR can be achieved through operating the APDs at decreased temperature. Figure 2-9 shows the measured DCR at 2-V overbias for 37- $\mu$ m-diam pixels from three different wafers at temperatures between 130 and 290 K. By cooling to 210 K, the DCR drops to <50 kHz for all three detectors. The generation current in the device from wafer 3 is more dominant than in the other two APDs because of shorter carrier lifetime in the InGaAsP absorber layer in that wafer. Operational temperatures above 210 K (–63°C) are easily achievable with thermoelectric coolers, making these detectors potentially useful for many applications.

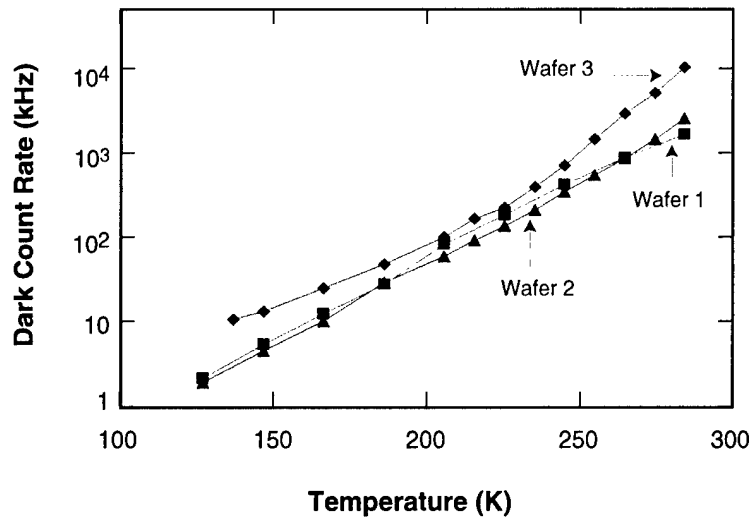


Figure 2-9. Temperature dependence of dark count rate at 2-V overbias for 37- $\mu$ m-diam detectors from three wafers.



Figure 2-10. Image recorded in indoor 60-m range with  $4 \times 4$  array of InGaAsP/InP Geiger-mode APDs in the Gen I Ladar system.

Variation in breakdown voltage across  $4 \times 4$  arrays is found to be  $<0.2$  V at all temperatures, allowing operation of a full array with a single bias voltage. To evaluate the performance of one of these  $4 \times 4$  arrays for three-dimensional imaging, an array was placed in the focal plane of a scanning Ladar brassboard system that utilizes a pulsed microchip Nd:YAG laser transmitter (Laser and Sensor Applications Group, MIT Lincoln Laboratory). External arming and timing circuitry control the array bias and measure the return time of received photons to within  $\sim 75$  ps. The APD array was operated at  $10^\circ\text{C}$ . Shown in Figure 2-10 is an image of several targets placed at a range of  $\sim 60$  m. This  $128 \times 128$  image was

recorded by tiling the instantaneous field of view of the  $4 \times 4$  array. Multiple  $128 \times 128$  frames were coincidence processed to improve image quality. The range is color coded in the figure to match the ~2-m range window occupied by the targets. This is the first demonstration of the capability of these InGaAsP/InP Geiger-mode APD arrays for three-dimensional imaging.

K. A. McIntosh	J. P. Donnelly
D. C. Oakley	A. Napoleone
S. D. Calawa	L. J. Mahoney
K. M. Molvar	E. K. Duerr
S. H. Groves	D. C. Shaver

### 2.3 ADVANCES IN THERMOELECTRIC MATERIALS AND DEVICES USING MOLECULAR BEAM EPITAXY, THERMOELEMENT ARRAYS, AND NOVEL ON-CHIP CHARACTERIZATION

Thermoelectric (TE) materials and devices are of interest for remote power generation and cooling applications. The suite of commercially available TE materials offers energy-conversion-efficiency values that are smaller than desired for such applications because the TE properties of those materials are not sufficiently large. However, the incorporation of low-dimensional quantum-dot superlattice (QDSL) heterostructures can cause the TE properties of a material to change [13]. QDSL materials therefore offer the potential for more widespread use of TE devices because of possibly increased energy-conversion efficiency. To be practical in these TE power generation and TE cooling applications, these QDSL materials must be amenable to processing such that high-density arrays with large fill factor can be readily formed and interconnected with low-resistance electrical contacts.

The QDSL materials are prepared in film form by molecular beam epitaxy (MBE). The MBE proceeds by thermal evaporation, controlled by mechanical shutters, from the solid source parent compounds (PbTe, PbSe, SnTe, and SnSe). Pure PbTe is first deposited as a thin buffer layer on  $\langle 111 \rangle$  barium fluoride. PbSe grows on PbTe in the Stranski-Krastanow mode, which results in the growth of tetrahedron-shaped quantum-dot structures, as shown in Figure 2-11. PbTe deposition then serves to replanarize the growth surface for subsequent PbSe quantum-dot deposition. This cyclical deposition process of alternating layers of PbSe dots and PbTe replanarizing spacer layers is repeated until the desired QDSL film thickness  $L$  is obtained.

Arrays of thermoelements are obtained from the films by photolithography and etching. The mask currently used for the photolithography defines thermoelements having a circular cross section with an area  $A$  of  $7.1 \times 10^{-4} \text{ cm}^2$ . The contact metallurgy used is 500-nm gold/50-nm nickel/500-nm gold. The Au/Ni/Au pads serve as efficacious etch masks after removal of the photoresist material because the pads are unaffected during the etching process. As shown in Figure 2-12, the portion of the QDSL film not covered by the metal pads is removed by the etching process down to the barium fluoride substrate, and a freestanding array of thermoelements results.

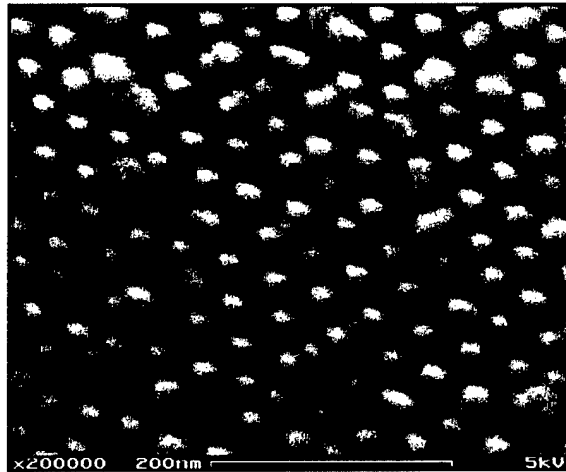


*Figure 2-11. Electron microscope image of tetrahedral PbSe quantum dots on the surface of PbTe.*



*Figure 2-12. Electron microscope image of individual thermoelements obtained by metallization and etching.*

Arrays of TE power generation or TE cooling devices are formed by series electrical interconnections between  $p$ - and  $n$ -type thermoelements. For TE power generation devices, a temperature difference causes electrical current to flow. For TE cooling devices, the application of an electrical current  $I$  from the  $n$ - to the  $p$ -type thermoelement causes Peltier heat to be absorbed at the metal “cold junction” interconnect between them. The electrical resistance of these devices includes the electrical resistivity of the  $p$ - and  $n$ -type thermoelements,  $\rho_p$  and  $\rho_n$ , respectively, and of the metal cold junction as well as the contact resistance  $R_c$  to the thermoelements.

For optimized energy-conversion efficiency, the resistive heating within the metal cold junction and the contacts to the thermoelements must be made negligible compared to that within the thermoelements. Ignoring the small resistive heating within the metal cold junction of a solitary  $n$ -type metal  $p$ -type thermoelement allows one to write:  $I^2\rho_n(L/A) + I^2\rho_p(L/A) \gg I^2(R_c(p) + I^2R_c(n))$ . Simplifying yields the condition that should be met for TE devices:  $(\rho_n L + \rho_p L) \gg (R_c + R_c)$ . For QDSL materials,  $L$  is on the order of  $100\ \mu\text{m}$ . This suggests that the specific contact resistance  $\rho_c$  ( $\rho_c = R_c A$ ) should be on the order of  $10^{-7}\ \Omega\cdot\text{cm}^2$ . This criterion emphasizes the importance of the specific contact resistance when considering device geometry having a small value for  $L$ , such as that of the present work.

Stopping the etching process midway allows for measurement of the specific contact resistance by a new technique. The new technique is a variation of the conventional transmission line technique [14]. In the conventional technique, a co-linear array of contact pads is deposited having a varying spacing between pads. The new technique makes use of the variable distance between pads that are non-co-linear.

To confirm that the specific contact resistance is determined correctly by the new non-co-linear technique, a set of contacts having the same metallurgy was deposited in both the conventional co-linear and new non-co-linear patterns on  $n$ -type material. The data shown in Figure 2-13 are the resulting measurements taken from the co-linear and non-co-linear sets of pads. The data points for each technique are fit using a linear extrapolation, and the contact resistance is determined by the intercept. The specific contact resistance is then calculated by multiplying the experimentally measured contact resistance by the contact area.

Both the non-co-linear technique and the conventional transmission-line technique determined the same value for the specific contact resistance. This confirms that the measurement of the specific contact resistance by the new non-co-linear technique is accurate. The new non-co-linear technique is a powerful characterization technique for the present device fabrication technology because it allows specific contact resistance measurement on the array of thermoelements forming the TE power generation device or cooling device itself.

When a brief plasma cleaning process is added prior to the Au/Ni/Au metals deposition, an important finding is obtained, as demonstrated in Figure 2-13. The specific contact resistance is found to decrease to the order of  $7 \times 10^{-8}\ \Omega\cdot\text{cm}^2$ . This is significant because it appears to satisfy the criterion that the resistive heating at the electrical contacts should be negligible compared to that within the thermoelements. The interpretation of this result is that the plasma cleaning removes organic contamination and disrupts the surface oxide on the QDSL material. The disrupted surface oxide would be expected to promote the interdiffusion of the contact material with the QDSL material, causing reduced electrical contact resistance.

In conclusion, PbSnTeSe QDSL materials have been grown by MBE. Films of these materials were used to form arrays of individual thermoelements with a high fill factor. A novel on-chip characterization technique to determine the specific contact resistance is presented. The new technique is robust and useful for materials and process characterization in real time. Specific contact resistance values as low as  $7 \times 10^{-8}\ \Omega\cdot\text{cm}^2$  can be obtained when incorporating a plasma cleaning process prior to the deposition of the contact

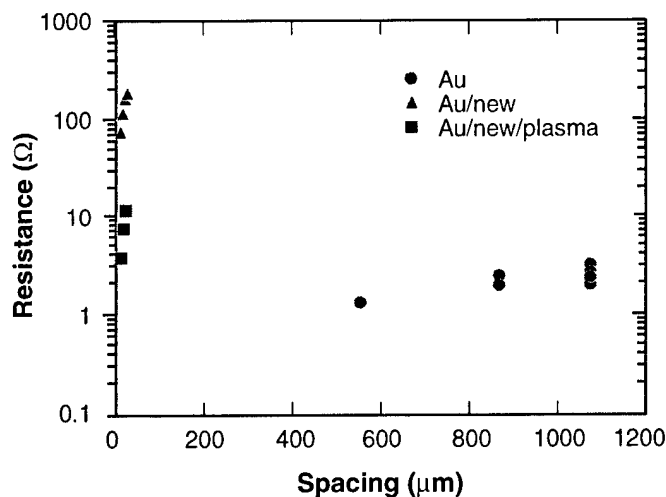


Figure 2-13. Comparison between conventional co-linear and new non-co-linear transmission line techniques for determination of specific electrical contact resistance.

metals. This value is significant because it demonstrates feasibility to fabricate new classes of TE cooling and TE power generation devices using this electrical contact technology with this new class of materials.

P. J. Taylor  
T. C. Harman  
L. J. Mahoney

## REFERENCES

1. P. F. Baldasaro, J. E. Reynolds, G. W. Charache, D. M. DePoy, C. T. Ballinger, T. Donovan, and J. M. Borrego, *J. Appl. Phys.* **89**, 3319 (2001).
2. J. S. Ward, A. Duda, M. W. Wanlass, J. J. Carapella, X. Wu, R. J. Matson, T. J. Coutts, and T. Moriarty, *AIP Conf. Proc.* **401**, 227 (1997).
3. D. M. Wilt, N. S. Fatemi, P. P. Jenkins, V. G. Weizer, R.W. Hoffman, Jr., R. K. Jain, C. S. Murray, and D. Riley, *AIP Conf. Proc.* **401**, 237 (1997).
4. G. W. Charache, D. M. DePoy, P. F. Baldasaro, and B. C. Campbell, *AIP Conf. Proc.* **321**, 339 (1996).
5. I.-H. Tan, C. Reaves, A. Holmes, Jr., E. L. Hu, J. E. Bowers, and S. DenBaars, *Electron. Lett.* **31**, 588 (1995).

6. F. Omnes, J.-C. Guillaume, G. Nataf, G. Jager-Waldau, P. Vennegues, and P. Gibart, *IEEE Trans. Electron Devices* **43**, 1806 (1996).
7. R. H. Horng, D. S. Wu, S. C. Wei, C. Y. Tseng, M. F. Huang, K. H. Chang, P. H. Liu, and K. C. Lin, *Appl. Phys. Lett.* **75**, 3054 (1999).
8. H. C. Lin, W. H. Wang, K. C. Hsieh, and K. Y. Cheng, *Electron. Lett.* **38**, 516 (2002).
9. C. A. Wang, H. K. Choi, and G. W. Charache, *IEE Proc.-Optoelectron.* **147**, 193 (2000).
10. X. Wu, A. Duda, J. J. Carapella, J. S. Ward, J. D. Webb, and M. W. Wanlass, *AIP Conf. Proc.* **460**, 517 (1999).
11. M. B. Clevenger, C. S. Murray, S. A. Ringel, R. N. Sacks, L. Qin, G. W. Charache, and D. M. DePoy, *AIP Conf. Proc.* **460**, 327 (1999).
12. Single Photon Counting Module SPCM-AQR Series data sheet (PerkinElmer Optoelectronics, Quebec, Canada).
13. T. Harman, P. J. Taylor, M. P. Walsh, and B. E. LaForge, *Science* **297**, 2229 (2002).
14. D. K. Schroder, *Semiconductor Material and Device Characterization*, 2nd ed. (Wiley, New York, 1998), p. 120.





### 3. SUBMICROMETER TECHNOLOGY

#### 3.1 DIAMOND OPTICALLY SWITCHED SCHOTTKY DIODES

Recent advances in diamond epitaxial growth techniques [1] at the Naval Research Laboratory (NRL) have enabled the growth of diamond layers with both a record low *p*-type doping,  $1 \times 10^{14}$  to  $1 \times 10^{16} \text{ cm}^{-3}$ , and compensation  $\sim 1 \times 10^{13}$ . Under a Cooperative Research and Development Agreement with DMC Corporation, we are exploring new devices made possible by these improvements in the quality of the diamond. Schottky diodes with breakdown voltages in excess of 6 kV, which is the highest voltage for Schottky diodes on any semiconductor [1], have been fabricated on this material. Here, we describe a novel optically switched device developed using this material.

Type Ib diamond, which is used as the substrate for this epitaxial diamond, contains substitutional nitrogen atoms that form a deep donor in diamond,  $\sim 2 \text{ eV}$  below the conduction band [2]. These diamonds are so insulating that once the nitrogen atom donates its electron to the conduction band and becomes positively charged, it can remain in this nonequilibrium state for days. When these diamonds are used for vacuum cathodes, emission currents can be changed by orders of magnitude by pre-ionizing the nitrogen impurities before the required voltages for emission are applied [3].

The interaction of these high-quality epitaxial diamond layers with their type Ib diamond substrates results in the novel properties exhibited by these devices. Charge exchange between the nitrogen in the substrate and the boron in the epitaxial layer modulates the conductivity of the layers. Although these impurities are physically separated, incandescent light ionizes the nitrogen atoms in the substrate producing photoelectrons. Under an externally imposed electric field, the electrons drift, forming a positive space charge layer in the substrate. Once this happens, the resulting internal electric field, produced by this space charge, sweeps out the positive mobile charge carriers, holes, from the epitaxial layer making it insulating.

If the diamond is illuminated with near-band-gap radiation, then photogenerated holes and electrons in the diamond will neutralize the internal electric field and the epitaxial layer will fill with holes and become conductive. Once the conductivity of the layer is established, it will remain in the same state for days if kept in the dark.

The switching between the conductive and insulating states is determined by the wavelength of the optical radiation. Photons from an incandescent quartz halogen tungsten lamp [4] have sufficient energy,  $>2 \text{ eV}$  ( $<600 \text{ nm}$ ), to photoionize nitrogen atoms, promoting electrons to the conduction band, but insufficient energy,  $<4 \text{ eV}$ , to neutralize the same atoms with electrons from the valence band. Thus, an incandescent lamp allows for the production of a positive space charge and the insulating state.

Radiation from a Hg(Ar) spectral calibration lamp emits photons with energy in excess of 4 eV (300–184 nm) [4]. However, much of this radiation is above 6 eV ( $<200 \text{ nm}$ ), which is heavily absorbed by

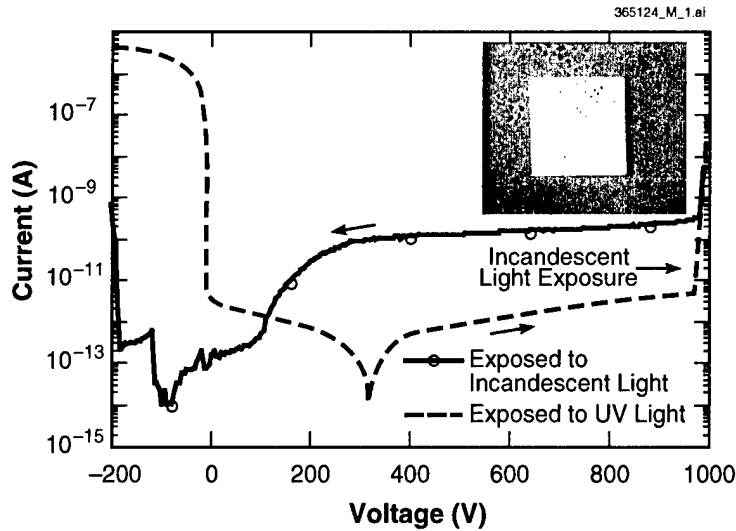


Figure 3-1. Current-voltage curve of Schottky diode taken in the dark. The dashed curve (in the high forward conduction state) starting at  $-200$  V was taken after exposing the diode to uv light. When the bias voltage reached  $985$  V, the diode was illuminated with incandescent light. The light was turned off and the voltage was stepped back from  $1000$  to  $-200$  V, as shown by the solid line. The inset is an optical micrograph of  $\sim 9\text{ }\mu\text{m}$  of an epitaxial diamond layer on a  $4 \times 4\text{-mm}$  type Ib diamond substrate. The rough surface is the result of polishing damage in the original diamond substrate growing into the epitaxial layer. The central square region is a Schottky diode consisting of  $50\text{ nm}$  of Cr patterned into a  $100 \times 100\text{-}\mu\text{m}$  square.

diamond [5] and cannot affect the charge state of the nitrogen atoms at the epitaxial layer–type Ib diamond substrate interface. This leaves only photons with energies below the band gap of diamond, the primary spectral lines at  $253\text{ nm}$ , and the secondary lines at  $265$ ,  $284$ , and  $302\text{ nm}$ . These spectral lines are believed to be responsible for establishing the conductive state by neutralizing the nitrogen atoms with electrons from the valence band.

Lightly boron doped homoepitaxial diamond layers, with a thickness of  $9\text{--}10\text{ }\mu\text{m}$ , were grown on type Ib synthetic diamonds at NRL using microwave plasma-enhanced chemical vapor deposition [1]. Schottky diodes, which were used to apply an external field and measure the conduction state, were formed on these layers and consisted of  $50\text{ nm}$  of electron-beam-evaporated Cr patterned into  $100\text{-}\mu\text{m}$  squares using standard lithography, as shown by the inset in Figure 3-1.

Several diodes were tested and all had breakdown voltages in excess of  $1100\text{ V}$  and leakage currents  $<10\text{ pA}$  at  $1100\text{ V}$ , as previously reported on similar diamond layers [1]. The diode's current-voltage (I-V) curve depends on previous biasing and light exposure, as shown in Figure 3-1. When light from a quartz halogen tungsten lamp,  $\sim 20\text{ mW cm}^{-2}$ , illuminates the diode while being biased to less than  $-200\text{ V}$  or above  $500\text{ V}$ , the diode becomes nonconductive when forward biased in the dark. Ultraviolet illumination

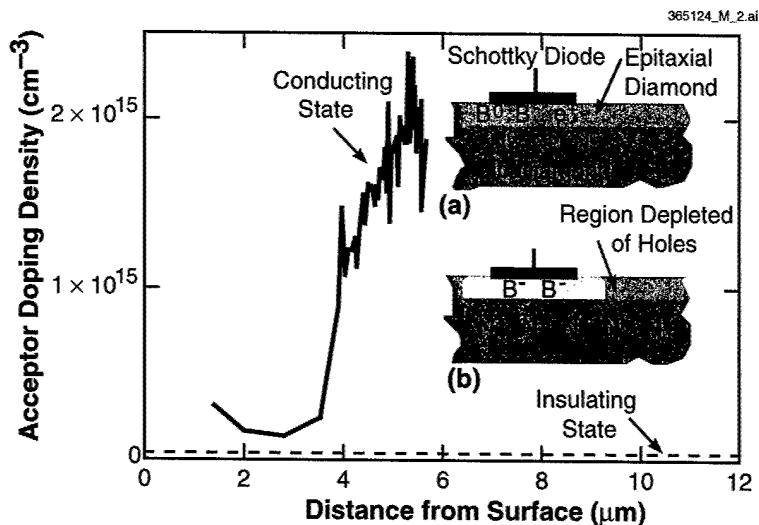


Figure 3-2. Acceptor density under the Schottky diode as determined by capacitance-voltage measurements. The solid curve, for a diode in the conductive state, was obtained after the diode was exposed to uv light. The dashed curve, for the same diode in the insulating state, where the active acceptor density is  $<10^{13} \text{ cm}^{-3}$ , was obtained after being biased to 1000 V and exposed to incandescent light. The pictorial insert shows two drawings of an epitaxial layer on a type Ib diamond substrate, contacted with a Schottky diode. (a) Schottky diode in the conducting state where the diamond substrate contains no positive charge and the epitaxial layer contains neutral ( $B^0$ ) and ionized ( $B^-$ ) boron atoms and mobile holes ( $e^+$ ). (b) Schottky diode in the insulating state where the substrate contains positively charged nitrogen atoms ( $N^+$ ) and no mobile holes in the epitaxial layer.

from an unfiltered Hg(Ar) lamp, independent of the bias during exposure, causes the diode to conduct when forward biased. The increase in forward current remained when diodes were again tested in the dark. A maximum current ratio between the conductive and insulating states of  $10^7$  was obtained at a forward bias of -50 V. This optical effect varied over the epitaxial layer and is believed due to the layer's variation of thickness and doping. The I-V curve shown in Figure 3-1 was obtained by first exposing the diode to near-band-gap uv radiation for ~10 s, putting the diode in the high forward conduction state, and then sweeping the voltage from -200 to 985 V in the dark. While the voltage was swept from 985 to 1000 V the diode was illuminated with a below-band-gap tungsten halogen lamp, which caused the leakage current to increase from  $2 \times 10^{-12}$  to  $8 \times 10^{-8}$  A. The voltage was then swept from 1000 to -200 V in the dark in the insulating, low forward conduction state.

Capacitance-voltage (C-V) measurements on the Schottky diodes were used to determine the hole densities [1] both for those holes attached to boron acceptors and those in the valence band. A comparison of the C-V measurements of the same diode in the conducting and insulating states is shown in Figure 3-2. When the diode is in the conductive state, acceptor concentration was measured to be  $\sim 2 \times 10^{15} \text{ cm}^{-3}$ . The low acceptor concentration for the first 4  $\mu\text{m}$  of the epitaxial layer is the result of the boron atoms being

compensated by hydrogen impurities [6],[7]. When the diode is placed in the insulating state, there is no measurable concentration of holes, because they have been swept out of the region under the diode by the built-in electric field.

M. W. Geis	J. C. Twichell
K. E. Krohn,	T. M. Lyszczarz
J. M. Lawless, Jr.	J. E. Butler*
S. J. Deneault	D. D. Flechtner*
M. F. Marchant	R. Wright*

### 3.2 X-RAY ZONE PLATE FABRICATION

X-ray microscopy offers nondestructive three-dimensional imaging at resolutions exceeding that of optical microscopy. In an x-ray microscope, the zone plate is the diffractive optical component that functions as the objective lens. The resolution that can be achieved by a zone plate is roughly equal to the width of the zone plate's outer zones. In addition, the thickness and composition of the zone plate determine the zone plate's efficiency. For good performance, it is therefore necessary to create very fine structures (45 nm) with a high aspect ratio in a dense material, such as gold. Under a Cooperative Research and Development Agreement with Xradia Inc., we have been developing the lithography technology for zone plate fabrication.

The 45-nm dense-feature patterning requirement for these zone plates exceeds the capabilities of current optical lithography tools, and we therefore used high-resolution electron-beam lithography for this task. To optimize the patterning, a lithography process bias of 10 nm per side was used, that is, the region exposed in each ring was 20 nm smaller than the final feature size. This biasing improves the feature size control by accounting for the finite width of the beam and the resolution of the resist. Because of the difference between the exposed size and the desired feature size, it is necessary to modify the exposure dose. This correction is a simple geometric one: a 50-nm feature exposed 30 nm wide gets an increase in dose of 66%. Because the feature sizes vary throughout a zone plate, this correction varies across a zone plate; and 14 levels of correction, or shot ranks, were used in each zone plate. A typical base dose for the final zone plates fabricated on membranes was around  $750 \mu\text{C}/\text{cm}^2$ . Figure 3-3 shows a scanning electron micrograph of 45-nm features in a zone plate patterned in polymethyl methacrylate (PMMA) resist.

To create high aspect ratio structures the trilayer resist structure shown in Figure 3-4 was used. The structure consists of a thick polymer layer (500–800 nm of organic antireflection coating from Brewer Scientific, or a proprietary resist), coated with a thin metal (6 nm of titanium), coated with a thin imaging resist (50 nm of PMMA). The thin imaging resist allows very high resolution imaging to be achieved,

---

\*Author not at Lincoln Laboratory.

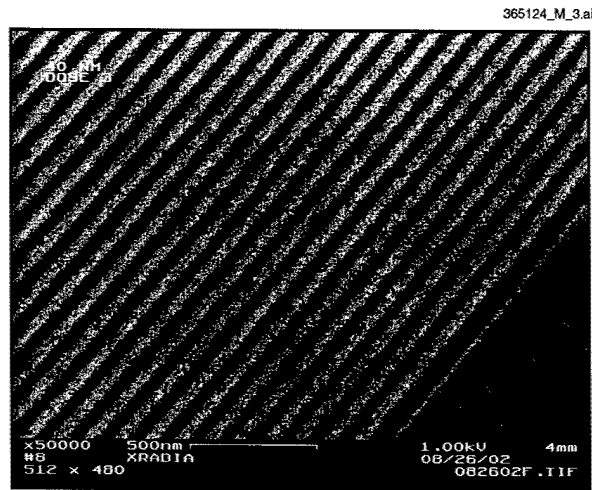


Figure 3-3. Scanning electron micrograph of 45-nm-wide outer zones of zone plate patterned in polymethyl methacrylate (PMMA) resist.

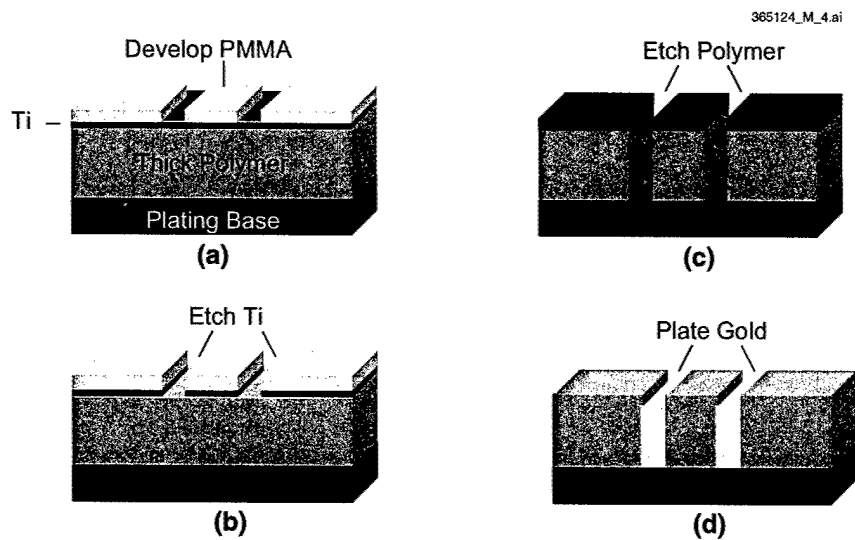


Figure 3-4. Process flow for zone plate fabrication with a trilayer resist: (a) pattern PMMA imaging layer, (b) etch Ti using PMMA mask, (c) etch thick polymer layer using Ti mask to form mold, and (d) plate gold into polymer mold.

while the rest of the resist structure allows the transfer of the pattern into a thick material. The pattern transfer through a trilayer resist structure involves two selective etches. First, a short reactive ion etch (RIE) with  $\text{BCl}_3$  is used to transfer the pattern from the thin imaging resist into the Ti layer. Next, another RIE step is used to transfer the pattern into the thick resist layer. For this step,  $\text{O}_2$ , which is highly etch selective for the organic polymer over the Ti, is used as the RIE gas. The high aspect ratio structures now in the polymer serve as a form for the creation of the final gold structures by electroplating. Before electroplating, the remaining Ti is removed by a short RIE, and after electroplating the polymer is removed by another  $\text{O}_2$  etch.

Initial sample preparation, including depositing the plating base and thick polymer layer, was done by Xradia. Once the sample arrived at Lincoln Laboratory, it was baked at  $185^\circ\text{C}$  for 30 min and then immediately coated with 6 nm of Ti using electron-beam evaporation. The sample was then spin coated with 950 000 molecular weight PMMA. The 2% PMMA, dissolved in anisole, was spun at 5700 rpm, to give the 50-nm-thick layer. Post-apply baking was done at  $160^\circ\text{C}$  for 15 min on a hotplate. After exposure, the samples were developed in a 1:3 mixture of methyl isobutyl ketone : isopropanol (MIBK:IPA) for 20 s, followed by a rinse for 30 s in IPA. After fabricating the PMMA structure at Lincoln Laboratory, the samples were sent to Xradia for the etching and electroplating steps outlined above. With the use of this process, zone plates 10 times as thick as the width of their finest features were created in gold. Xradia has used the completed zone plates in a prototype x-ray microscope and has produced three-dimensional images of the multilayer metallization on integrated circuit samples. Spatial resolution better than 80 nm has been achieved with this system.

S. J. Spector                      D. Lennon  
S. Deneault

## REFERENCES

1. J. E. Butler, M. W. Geis, K. E. Krohn, J. Lawless, Jr., S. Deneault, T. M. Lyszczarz, D. Flechtner, and R. Wright, to be published in *Semicond. Sci. Technol.*
2. A. T. Collins and E. C. Lightowers, in *The Properties of Diamond*, J. E. Field, ed. (Academic, London, 1979), pp. 79–105.
3. M. W. Geis, J. C. Twichell, and T. M. Lyszczarz, *J. Vac. Technol. B* **14**, 2060 (1996).
4. Oriel Instruments Pencil Style Spectral Calibration Lamps (Spectra-Physics, Stratford, Conn.). Retrieved 29 January 2003 from <http://www.oriel.com/down/pdf/01021.pdf>.
5. *Handbook of Optical Constants of Solids*, E. D. Park and H. R. Phillips, eds. (Academic, New York, 1985), pp. 670–673.
6. M. W. Geis, N. N. Efremow, and J. A. von Windheim, *Appl. Phys. Lett.* **63**, 952 (1993).
7. R. Zeisel, C. E. Nebel, and M. Stutzmann, *Appl. Phys. Lett.* **74**, 1875 (1999).

## 4. BIOSENSOR AND MOLECULAR TECHNOLOGIES

### 4.1 CELL AND ASSAY ANALYSES IN CANARY BIOSENSOR DEVELOPMENT

In the development of the CANARY (Cellular Analysis and Notification of Antigen Risks and Yields) biosensor [1], we have studied background contamination resistance using a dry aerosol collection device. In addition, the performance of ready-to-use B cells that have been frozen and stored for extended periods [2] has been further analyzed, and in collaboration with Professor Malcolm Potts of Virginia Tech, preliminary results have been obtained from studies of desiccation and storage of B cells.

To assess the effects of real contaminants on the CANARY assay, a dry aerosol collection device was used to collect aerosol background samples. The simple collection method exploits the relatively high momentum of particles to force them to impact on a dry surface where a fraction of the impacted particles are bound nonspecifically and retained. The basic concept and one of our collector prototypes are shown in Figure 4-1. A CANARY sensor can be used to identify bioagents collected using dry impaction without further processing, since this method localizes bioagents to the tube surface thereby eliminating the need to pre-spin the sample for maximum performance. This collection method should also improve the sensitivity of the CANARY assay for small viruses that are not concentrated by a microcentrifuge. Dry impaction makes the CANARY assay protocol faster and simpler to perform (and automate) than the protocol used for liquid samples.

We have completed an analysis of the effects of typical background aerosol contaminants on CANARY identifier performance with respect to false-positive and false-negative rates. The results are

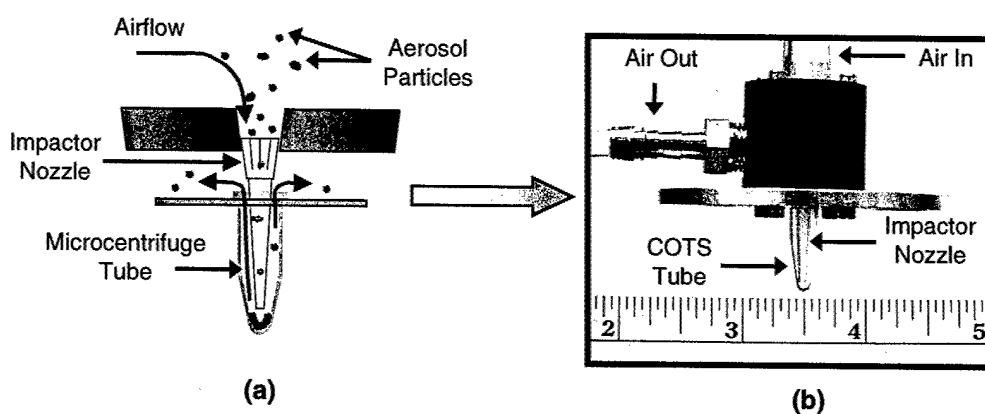


Figure 4-1. (a) Dry impaction concept and (b) prototype device. Inexpensive single-use impactors are envisioned that would include a downstream filter to prevent contamination of the (reusable) air pump that maintains the air flow through the impactor. This design is readily scalable for parallel collection into multiple commercial off the shelf (COTS) tubes.



**TABLE 4-1**  
**Dry-Impacted Aerosol Samples Analyzed with the CANARY Assay**

Aerosol Sample	False Positives	False Negatives (500 cfu)
Indoor	1/364 = 0.3%	0/34
Outdoor	2/328 = 0.6%	0/8

summarized in Table 4-1. Samples were collected from several indoor and outdoor locations for 5–10 min at an air flow rate of 5 L/min, and tested with two cell lines, one specific for *Yersinia pestis* and the other for *Bacillus anthracis*. The false-positive rate for indoor samples was 0.3% (1 in 364), and for outdoor samples 0.6% (2 in 328). A single set (84) of indoor samples caused a nonspecific high background that did not have the kinetic signature of a false positive, but which would have obscured the response to low levels of bioagent. However, this phenomenon appears to be rare as we have been unable to repeat it, even in the same location. To investigate if inhibitors might be present in dry-collected aerosols, 500 colony-forming units (cfu) of *Y. pestis* were added after aerosol collection, and then the sample was tested with *Y. pestis*-specific B cells. There were no false negatives in any of the 34 indoor or 8 outdoor samples tested in this manner.

B cells can be prepared for the CANARY assay, frozen and stored below  $-80^{\circ}\text{C}$ , thawed, washed, and used directly without any additional preparation. These cells can be used immediately after thawing or stored for up to a week at  $4^{\circ}\text{C}$  without any loss in sensitivity or speed. We have continued to analyze the performance of ready-to-use cells stored for extended periods in liquid nitrogen by thawing and testing them at one-month intervals. After three months of frozen storage the cells retain the ability to identify as little as 50 cfu of antigen. This improvement in cell preparation provides the user with a frozen reagent that requires no expertise and little handling prior to use.

Desiccation of B cells to provide long-term ambient-temperature storage has yielded very encouraging preliminary results. *Y. pestis*-specific B cells provided by Lincoln Laboratory were desiccated in Professor Potts' laboratory at Virginia Tech and shipped to us. Viable, responsive B cells have been recovered following desiccation under different conditions on six independent occasions. Figure 4-2(a) shows the response of cells desiccated with several different additives (dried on agarose, dried with glycan and glycerol, or no additives during desiccation), stored for nine days at room temperature, rehydrated, and then primed (treated with DMSO) and loaded (with coelenterazine) for the CANARY assay. The response of these cells to 500 000 cfu of *Y. pestis* compares favorably with undesiccated cells prepared and tested the same way (control B cells).

Figure 4-2(b) demonstrates that sensitivity can be completely recovered after desiccation and rehydration. In this experiment, B cells were treated with DMSO before desiccation, dried on agarose, and

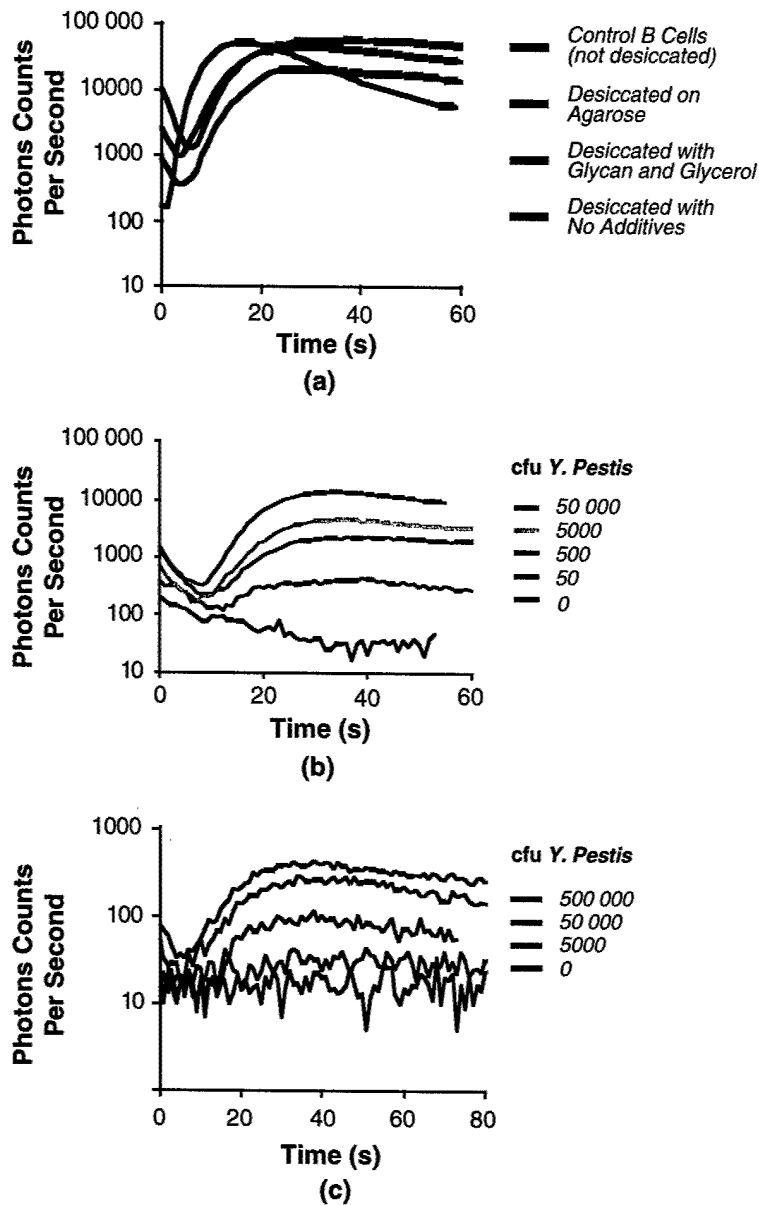


Figure 4-2. (a) Response to 500 000 colony-forming units of *Yersinia pestis* with B cells desiccated using different additives (dried on agarose, with glycan and glycerol, or with no additives), stored for nine days at room temperature, rehydrated, and primed and loaded for the CANARY assay; (b) dose response of B cells treated with DMSO, dried on agarose, and stored for two days at room temperature before rehydration and preparation for assay; and (c) response of B cells prepared for assay before desiccation and stored for two days.

stored for two days at room temperature. Following rehydration they were primed and loaded for the CANARY assay and can respond to as little as 50 cfu of *Y. pestis*.

As shown in Figure 4-2(c) we have also been able to recover active B cells that were primed and loaded for the assay before desiccation and required only rehydration before testing. This is the simplest case for end users; they would merely have to rehydrate the cells and load them into a sensor. Although the response of the cells is attenuated, the priming, loading, and desiccation conditions have yet to be optimized. These results demonstrate that dry storage and recovery of active B cells is a realistic goal.

M. S. Petrovick	J. D. Harper
R. H. Mathews	D. J. Blanchard
S. S. Lakdawala	

## REFERENCES

1. Solid State Research Report, Lincoln Laboratory, MIT, 2001:2, p. 25.
2. Solid State Research Report, Lincoln Laboratory, MIT, 2002:1, p. 21.

## 5. ADVANCED IMAGING TECHNOLOGY

### 5.1 DEEP-DEPLETION IMAGE SENSORS

A thick photon-absorbing region is generally desirable in silicon image sensors for certain applications, such as high-performance scientific and military missions. Thick active regions increase both the near-ir (800–1000 nm) sensitivity and the soft-x-ray response for energies above ~6 keV. However, these active regions must be kept depleted to minimize lateral thermal diffusion of the photocarriers. Carrier diffusion in undepleted regions can lead to loss of modulation transfer function and poor point-spread function. The two approaches traditionally utilized to increase depletion depth are to use high-resistivity substrate material and to raise the gate or photodiode biases of the device. Back-illuminated devices that are already fully depleted under normal biasing conditions can have improved point-spread response if the depletion layer fields are increased by these traditional techniques [1]. However, both have their limits, one because of the limits on the wafer resistivity available commercially and the other because of limits on the allowed bias voltages set by dielectric or junction breakdown. A third approach, biasing the substrate independently of the sensor circuitry, is described here. Although a thick, fully depleted *p*-channel charge-coupled device (CCD) with substrate bias has been described in literature [2], the design and biasing considerations for such a device have not been published. Here, we describe the device design issues and test results on an *n*-channel deep-depletion CCD using substrate bias.

The key to biasing the substrate is the electrical isolation of the circuit side of the device from the substrate by a depletion layer. This is illustrated in Figure 5-1 for the case of an *n*-channel CCD made on a *p*-type substrate. On low-resistivity silicon, the depletion edges are relatively shallow, and a conducting path exists between the channel stops and the substrate. This prevents any attempt to apply a substantial bias across the two. On high-resistivity substrates, on the other hand, the depletion layers not only penetrate deeper but also laterally and thus isolate the channel stops. When the depletion layer fields are sufficiently high, a potential barrier to holes is formed between the channel stop and substrate, and the substrate can be biased without drawing current. The structure is similar to a *p*-channel static induction transistor (SIT) [3], where the channel stops and substrate are the source and drain and the CCD gates and guard rings are the SIT gates.

It is relatively easy to isolate the channel stops when they are narrow (~2  $\mu\text{m}$  or less), as is usually the case in CCD pixels. However, the channel stops at the device perimeter or surrounding other circuit elements such as transistors may need to be wider, and in such cases the depletion layer fields need to penetrate far enough laterally to pinch off the parasitic hole current. Figure 5-2 illustrates the use of  $n^+$  regions, or guard rings, around the device perimeter and output transistors to further extend the lateral depletion. Generally, as the channel stop is made wider, the guard rings need to be wider and their bias  $V_{\text{gr}}$  raised to suppress the hole current.

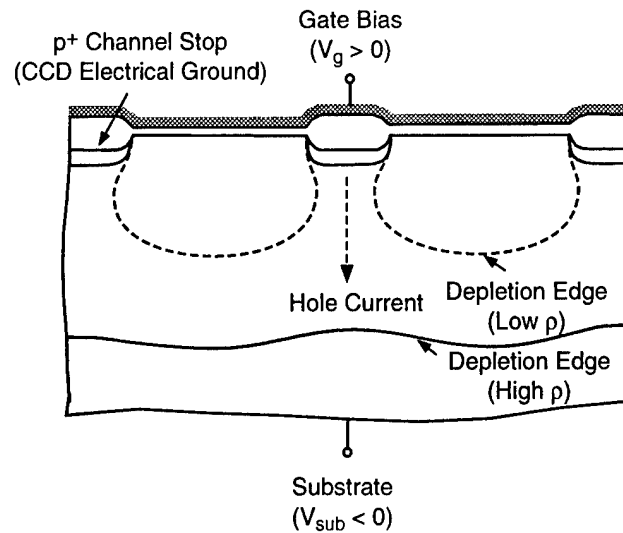


Figure 5-1. Depiction of cross section of charge-coupled device (CCD) showing depletion layer edges on low- and high-resistivity substrates.

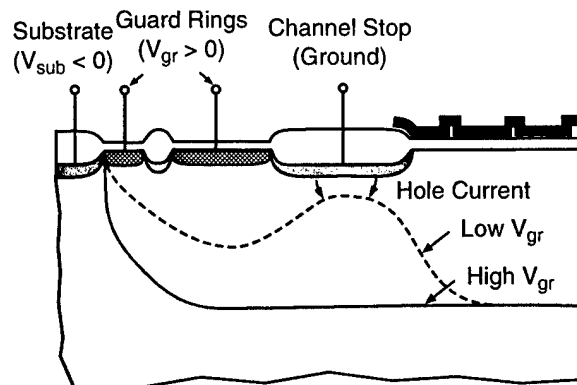


Figure 5-2. Illustration of substrate isolation issues at the perimeter of a device.

Figure 5-2 also illustrates another important feature of the design, namely, the ability to bias the substrate from the top or circuit side of the device. This has advantages for packaging because it keeps all input/output leads on the same side of the device and obviates the need for a special wire to be attached to the back surface. However, an issue that arises with this layout is the breakdown voltage between the guard ring and the substrate, since the potential difference between the two may be 50 V or more. For this reason,

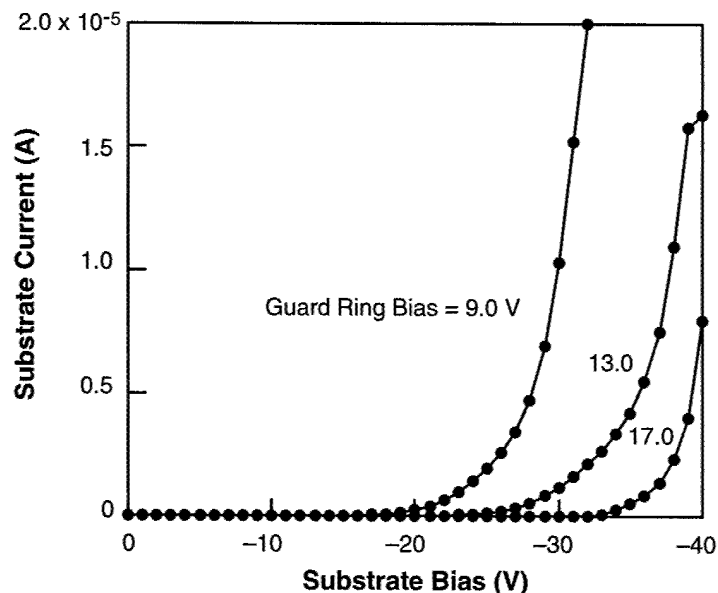


Figure 5-3. Measurement of hole current from device channel stops to substrate for various values of bias on the two inner guard rings.

two or more guard rings are placed around the perimeter, and the guard ring voltages stepped down from the inner to outer rings to distribute the voltage drop across more than one junction.

These ideas have been tested on a  $512 \times 512$ -pixel frame-transfer CCD with  $15\text{-}\mu\text{m}$  pixels. The outer channel stop surrounding the device was  $10\text{-}\mu\text{m}$  wide. Surrounding it were three guard rings, the inner one  $20\text{-}\mu\text{m}$  and the two outer ones  $15\text{-}\mu\text{m}$  wide. They were separated by  $5\text{-}\mu\text{m}$ -wide channel stop rings. To test the degree of electrical isolation, we measured the hole current from channel stop to substrate at varying guard ring biases, and some representative data are shown in Figure 5-3. In this case, the two inner guard rings were biased as shown, while the outer guard ring was left floating. The reset drains and the source and drain junctions of the output-amplifier transistors were biased to  $12\text{ V}$ . The data show that with sufficient guard ring bias the substrate can be biased as low as  $-40\text{ V}$  while keeping the hole current less than  $10\text{ }\mu\text{A}$ . Because of the strong dependence on guard ring voltage, we believe that the current in this data is originating from the  $10\text{-}\mu\text{m}$ -wide peripheral channel stop and not from the  $2\text{-}\mu\text{m}$ -wide channel stops within the pixel array.

To measure the depletion depth, we included a special test pattern for capacitance-voltage (C-V) measurements whose structure was identical to the CCD pixel array but with a single poly gate covering the entire device. The structure was surrounded by a single  $50\text{-}\mu\text{m}$  guard ring biased to  $20\text{ V}$ , and the gate was set to  $0\text{ V}$ . The data in Figure 5-4 show that a depletion depth of  $160\text{ }\mu\text{m}$  was achieved at a substrate

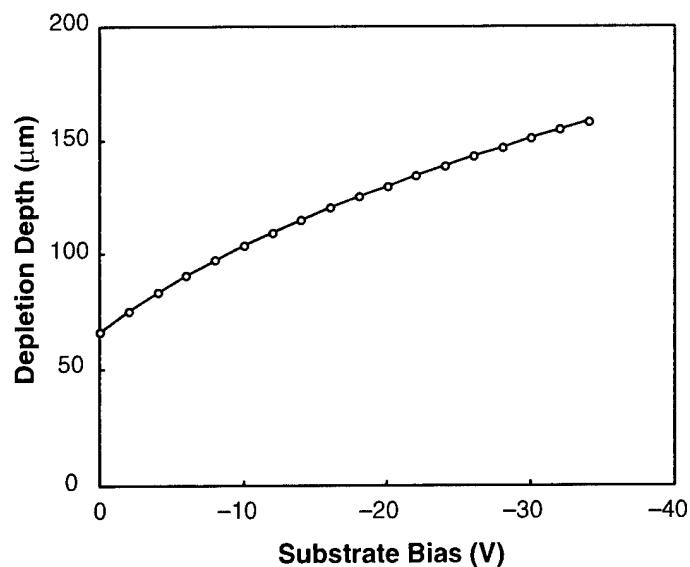


Figure 5-4. Depletion depth as a function of substrate bias from capacitance-voltage measurements on a special test pattern that represents the CCD pixel array.

bias of  $-34$  V. Further analysis of the C-V data shows that the substrate doping in this case was  $2 \times 10^{12} \text{ cm}^{-3}$ , or a resistivity of  $6900 \Omega\text{-cm}$ . Without substrate bias and with clocking voltages of about  $10$  V on the gates (the maximum normal level), we typically obtain depletion depths up to  $60\text{--}70 \mu\text{m}$ . Thus, the substrate bias has led to more than a twofold improvement in depletion depth.

B. E. Burke  
D. D. Rathman  
R. M. Osgood III

## REFERENCES

1. Solid State Research Report, Lincoln Laboratory, MIT, 2002:3, p. 23.
2. S. E. Holland, G. Goldhaber, D. E. Groom, W. W. Moses, C. R. Pennypacker, S. Perlmutter, N. W. Wang, R. J. Stover, and M. Wei, *International Electron Devices Meeting Technical Digest* (IEEE, Piscataway, N.J., 1996), p. 911.
3. J. Nishizawa, T. Terasaki, and J. Shibata, *IEEE Trans. Electron Devices* **22**, 185 (1975).

## 6. ANALOG DEVICE TECHNOLOGY

### 6.1 DOMAIN WALL MOTION EFFECTS ON HIGH-FREQUENCY PERMEABILITY OF FERRITES

From the earliest years of "soft" ferrite development, two frequency-dependent phenomena have been considered to establish the limits of their applicability in alternating magnetic fields  $H_{ac}$ . Neither, however, takes into account the influence of magnetic domain motion. In the unmagnetized state where magnetocrystalline anisotropy  $K_1$  dictates the directions of local magnetization vectors  $M_s$  in specimens with multiple domains, the coupling between  $H_{ac}$  and  $M_s$  ranges continuously between parallel (longitudinal) and perpendicular (transverse). In the analysis of permeability dispersion, the two effects are generally introduced as (i) the magnitude of the initial  $\mu_i$ , which is determined by the ease of magnetization rotation within the randomly oriented domains by  $H_{ac} \cdot M_s$  coupling, and (ii) the lowest frequency at which transverse  $H_{ac} \times M_s$  interactions occur through the gyromagnetic conversion constant  $\gamma$ . Here, domain wall resonance is analyzed and its influence on permeability contrasted with the effects of single-domain rotation and gyromagnetic resonance.

A number of influences were overlooked in the formulation of this elementary guideline. In theory at least, the dispersive decline of  $\mu_i$  from its initial value can be the result of the longitudinal nonresonant spin-lattice relaxation rate  $1/\tau$ , which is less than the gyromagnetic resonance frequency. The more important mechanism for high  $\mu_i$  in all but the infrequent examples of single-domain particles, however, is domain wall resonance. Domain walls can be shown to have mechanical-like properties of a forced damped harmonic oscillator that is characterized in terms of effective mass  $m_w$ , restoring force  $\alpha_w x$  when disturbed from equilibrium in the  $x$  direction, and motional damping force  $\beta_w(dx/dt)$  characterized by a damping relaxation time  $\tau_w$ . An equation of motion for domain walls of total surface area/volume  $\zeta_w$  under the action of a  $z$ -axis alternating magnetic field  $H_{ac}$  of angular frequency  $\omega$  is given by [1]

$$m_w \ddot{x} + \left( \frac{m_w}{\tau_w} \right) \dot{x} + \alpha_w x = 2M_s H_{ac} \cos(\omega t) \quad (6.1)$$

where  $\beta_w$  is replaced by  $m_w/\tau_w$ ,  $m_w = (1/4\pi)\gamma^{-2}(K_1/A)^{1/2}$ ,  $\alpha_w = 4K_1\zeta_w/6\pi$  for the more common case of  $K_1 < 0$ , and  $A$  is the wall exchange energy divided by the lattice parameter. From inspection of Figure 6-1, we reason that the wall displacement by  $H_{ac}$  produces a change in net magnetization of  $M_{ac} = 2M_s\zeta_w x$ , or in terms of susceptibility,

$$\chi_{ac} = \frac{M_{ac}}{H_{ac}} = \frac{2M_s\zeta_w x}{H_{ac}} \quad (6.2)$$



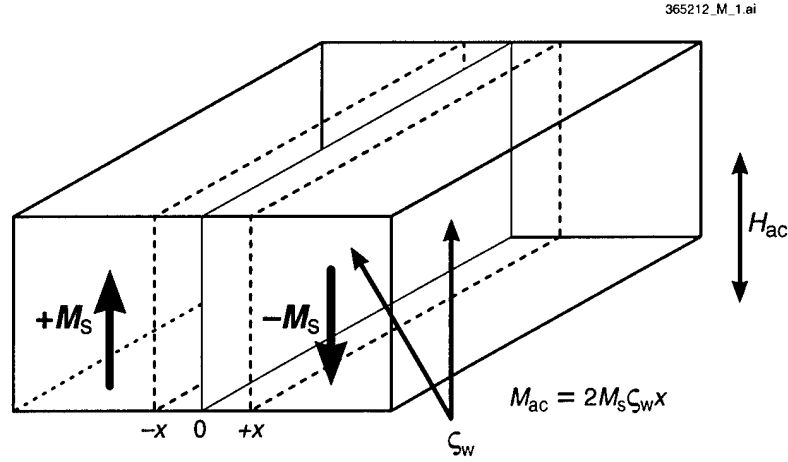


Figure 6-1. Model of domain wall displacement under the influence of a longitudinal ac magnetic drive field.

Therefore, we can now express Equation (6.1), after dropping the subscript ac, as

$$\ddot{\chi} + \left( \frac{1}{\tau_w} \right) \dot{\chi} + \omega_w^2 \chi = \frac{(2M_s)^2 \zeta_w}{m_w} \cos(\omega t) \quad (6.3)$$

where  $\omega_w^2 = (8/3)\gamma^2(AK_1)^{1/2}\zeta_w$ . It should be noted that  $\omega_w$  is dependent jointly on the wall exchange energy  $A$  (hence the Curie temperature), the anisotropy, and the disposition and density of the domain configuration.

The initial susceptibility from reversible wall movement is deduced directly from the solution of Equation (6.3), according to [2]

$$\chi_w = \frac{(2M_s)^2 \zeta_w}{m_w \sqrt{(\omega_w^2 - \omega^2)^2 + (1/\tau_w)^2 \omega^2}} \cos(\omega t - \varphi) \quad (6.4)$$

where

$$\tan \varphi = \frac{\omega}{\tau_w(\omega_w^2 - \omega^2)}$$

It can be easily shown that the maximum frequency  $\omega_d$  to avoid critical damping of the resonance (that allows a real value of  $\chi_w$ ) is determined by the minimum value of the denominator of Equation (6.4), which is given by

$$\omega_d^2 = \omega_w^2 - \frac{1}{2\tau_w^2} \quad (6.5)$$

Since  $\omega_w$  already increases with  $K_1$ ,  $A$ , and  $\zeta_w$ , we now conclude that the threshold for the collapse of the domain wall contributions to  $\chi_i$  is also dependent on  $\tau_w$ , which requires large values to allow the forced oscillation to remain below the critical damping limit of Equation (6.5).

Because  $\alpha_w$  can also be expressed as  $4M_s^2\zeta_w/3\mu_i$ , other useful relations can be deduced from Equation (6.4). For the initial value of  $\chi_w$  (at  $\omega = 0$ ),

$$\chi_w(0) = \frac{4M_s^2\zeta_w}{m_w\omega_w^2} = \frac{4M_s^2\zeta_w}{\alpha_w} = 3\mu_i \approx 12\pi\chi_i \quad (6.6)$$

As a consequence, an increase in  $\chi_i$  of a factor between 30 and 40 over the magnetization rotation value could be expected from reversible domain wall movement. Moreover, at  $\omega = \omega_d$  a peak in  $\chi_w$  occurs, with an increase over the initial value as estimated from the amplitude of Equation (6.4), according to

$$\frac{\chi_w(\omega_d)}{\chi_w(0)} = \frac{\omega_w^2\tau_w^2}{\sqrt{\omega_w^2\tau_w^2 - 1/4}} \approx \omega_w\tau_w \quad (\text{for } \omega_w\tau_w \gg 1) \quad (6.7)$$

The qualitative results of this analysis are sketched schematically in Figure 6-2, where it is suggested that the trade-off between high-permeability and high-frequency operations is also dependent on the spin-lattice relaxation time. Low wall damping (large  $t_w$  and  $\zeta_w$ ) promises superior low-frequency properties, but also an earlier onset of dispersion in multiple-domain specimens. Above the domain wall damping edge, the reduced permeability of single-domain rotation is still present provided that  $1/\tau > \omega_d$ . Amidst these conflicts lies the influence of  $K_1$ , which is also dependent on  $1/\tau$ . Slower relaxation usually means smaller  $K_1$ , higher  $\mu_i$ , and the earlier appearance of gyromagnetic loss effects because of a reduced value of the anisotropy field  $H_K$  ( $\sim K_1/M_s$ ).

In conclusion, the issue of domains walls for unmagnetized materials can be resolved into a simple rule: (i) multiple domains, low  $K_1$ , high  $\tau$  for low frequencies, (ii) single domain, high  $K_1$ , low  $\tau$  for high frequencies. For microwaves, where  $\omega$  is above the dispersion region, the upper edge of the gyromagnetic resonance region becomes a concern, such that the low- $K_1$ /high- $\tau$  combination can be preferred, unless very high  $K_1$  hexaferrites are desired for millimeter waves.

G. F. Dionne

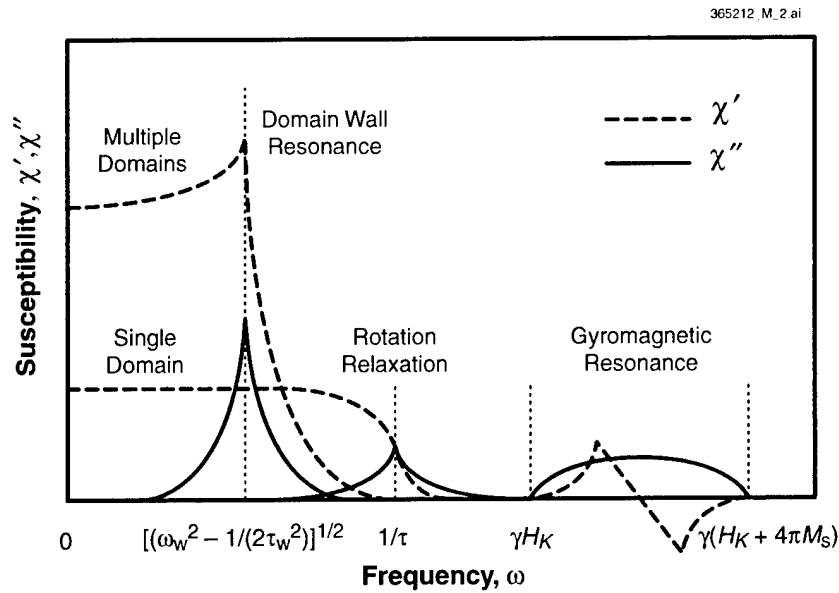


Figure 6-2. Schematic diagram of permeability variations as a function of frequency caused by various magnetic damping actions.

## REFERENCES

1. S. Chikazumi, *Physics of Magnetism* (Wiley, New York, 1997), p. 574.
2. R. A. Becker, *Introduction to Theoretical Mechanics* (McGraw-Hill, New York, 1954), p. 144.

## 7. ADVANCED SILICON TECHNOLOGY

### 7.2 LOW-TEMPERATURE OXIDE-BONDED THREE-DIMENSIONAL INTEGRATED CIRCUITS

A silicon-on-insulator (SOI) based three-dimensional (3D) integrated circuit process has previously been described [1], which vertically stacks and interconnects active circuit layers and demonstrates the viability of the technology by the fabrication of adhesive-bonded two-tier CMOS ring oscillators and  $64 \times 64$  active pixel sensors. The vertical interconnections were formed with sputtered aluminum and had a minimum pitch of  $12 \mu\text{m}$ . The maximum working temperature of the adhesive bond,  $200^\circ\text{C}$ , restricted a further decrease of the interconnection pitch. To develop more complex 3D circuits, a low-temperature oxide-oxide bond process has been developed that permits the stacking and interconnecting of circuit layers with tungsten plugs of size and pitch approaching current 2D via designs. The oxide bonding process is also compatible with the  $400\text{--}500^\circ\text{C}$  anneals used to improve transistor properties that complete wafer fabrication. Here, we report the development of this process, including operational circuits and three-tier via chains fabricated using concentric vias, as shown in Figure 7-1.

The chemistry of bonding wafers covered with silicon dioxide films has been thoroughly described by many workers [2]–[4]. The two surfaces to be bonded must have a high density of hydroxyl (OH) groups present. When the surfaces are brought into contact, weak ( $\sim 0.45 \text{ eV}$ ) hydrogen bonds are created at the interface ( $\text{Si-OH}:\text{OH-Si}$ ). Heating the bonded wafer pair to temperatures  $>150^\circ\text{C}$  produces covalent bonds at the interface from the reaction  $\text{Si-OH}:\text{OH-Si} \rightarrow \text{Si-O-Si} + \text{H}_2\text{O}$ , with the Si-O bond having a bond energy of  $4.5 \text{ eV}$ .

The wafer bonding process begins with a chemical-mechanical polishing (CMP) step to planarize and smooth the deposited oxide surfaces to a roughness  $<0.4 \text{ nm rms}$  as measured by atomic force microscopy. The post-CMP film thickness is  $\sim 0.5 \mu\text{m}$ . The wafers are immersed in  $\text{H}_2\text{O}_2$  at  $80^\circ\text{C}$  for 10 min to remove any organic contaminants and to activate the surfaces, followed by a deionized water rinse and spin dry in room air. Wafers that do not require pattern alignment are placed face to face in a jig in room air and are held apart by shims. Center point contact is made and the shims are withdrawn. The contact wave propagates to the edge of the wafers ( $150\text{-mm}$  diameter) in about 15–30 s. The pair is then placed between two polished stainless steel discs on a hot plate for the silanol-to-siloxane conversion step. The bond strengths obtained are sufficient for the wafer pair to tolerate back-end-of-the-line (BEOL) processes.

After the thermal cycle has been completed the wafers are inspected for voids with an infrared camera. Surface energy measurements are made using the blade insertion technique described by Maszara et al. [5]. The crack length is corrected for infrared viewing by a recursive calculation. The error bars on the plots reflect the range for four data points on each wafer pair plus measurement error.

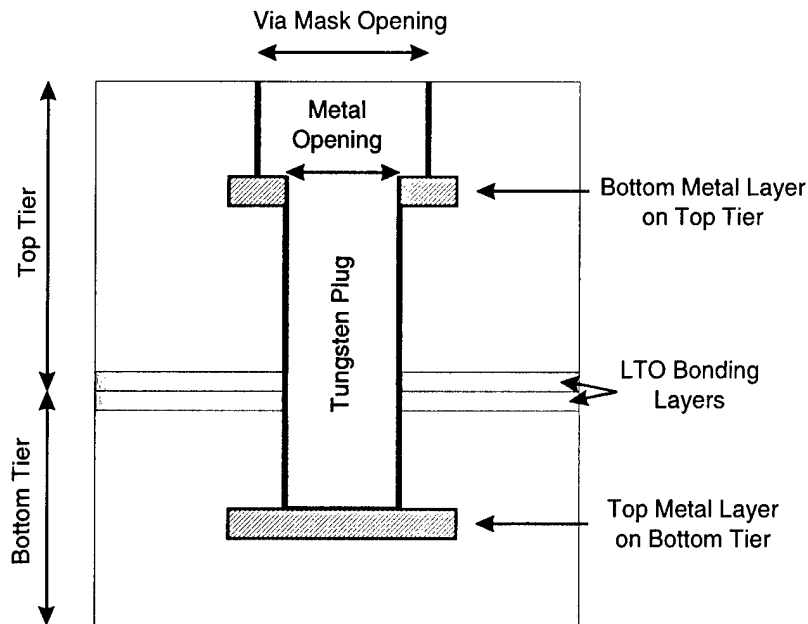


Figure 7-1. Concentric via cross section. This design requires only one mask as compared with the three used in earlier work [1].

We have compared bond quality using films deposited by plasma-enhanced (PE) chemical vapor deposition (CVD) from a tetraethoxysilane (TEOS) source (300°C) to low-temperature oxide (LTO) films deposited by low-pressure CVD (430°C) from silane and oxygen. Figure 7-2 is a plot of surface energy for wafer pairs bonded using a 300°C 8-h thermal cycle. Note that the LTO films have consistently higher surface energies than the PE TEOS films. Additionally, after substrate removal and a 500°C 1-h anneal small blisters appeared on the PE TEOS samples whereas the LTO samples were unaffected.

Surface energy and voided area were measured for LTO wafers bonded using temperatures of 150–500°C and times of 1–100 h. Figure 7-3 is an Arrhenius plot of the surface energy for 1- and 10-h samples. An activation energy of 0.14 eV is obtained from a data fit, which contrasts with data of Tong et al. [4] for hydrophilic native oxide surfaces (shown as a dashed line in Figure 7-3). At 150°C, there is a moderate increase in surface energy after a 100-h cycle, but no significant time dependence at higher temperatures. Void formation has a strong temperature dependence, as shown in Figure 7-4. The data indicate that it is desirable to bond at temperatures of 150–300°C to prevent void formation. Once the handle substrate has been removed after the thermal cycle, the wafer can be subjected to a temperature of 500°C without creating voids in the bonded films, suggesting that the silicon acts as a diffusion barrier for the trapped gas (presumably water) at the bond interface.

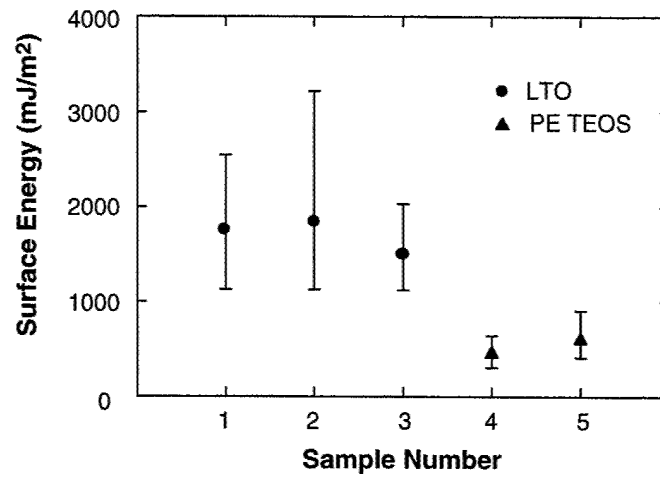


Figure 7-2. Surface energy of bonded wafer pairs as measured by the blade insertion/crack propagation method.

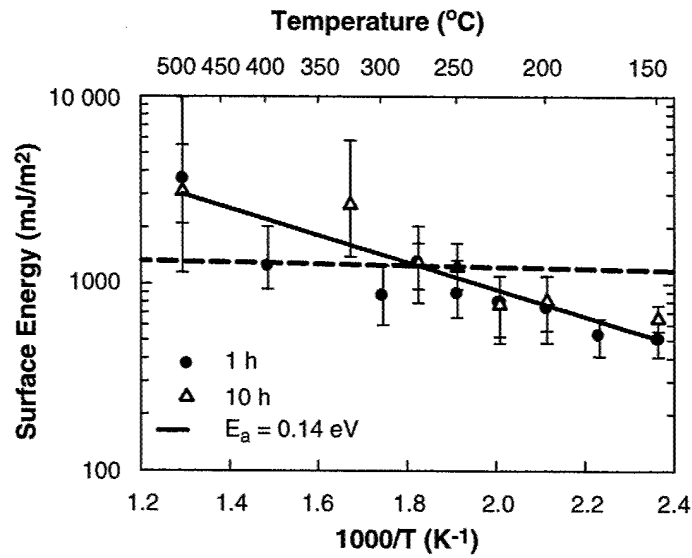


Figure 7-3. Arrhenius plot of surface energy vs bonding temperature for 1- and 10-h cycles. Data from [4] is shown as the dashed line.

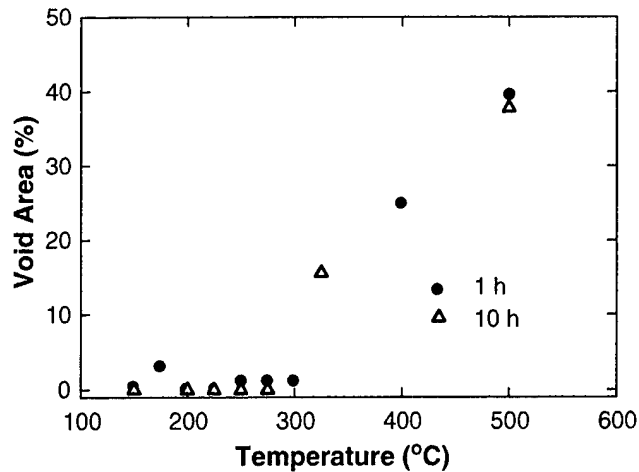


Figure 7-4. Percentage of bonded wafer area covered by voids as a function of bonding temperature.

For wafers that contain completed circuitry, a layer of LTO is deposited and the process described above is used to prepare the wafers for bonding. The wafers are aligned to each other using a modified Karl Süss MA-6 wafer aligner with infrared optics. Wafer-to-wafer alignment accuracy is better than  $2\text{ }\mu\text{m}$  with this tool. After the wafers have been aligned they are bonded by initiating contact at the center of the top wafer, and after 30 s the wafer pair can be removed from the aligner without disturbing the bond.

The handle silicon of the top wafer is removed by a wet chemical etch that is selective to the buried oxide. The inter-tier connections, referred to as concentric vias, are formed by aligning a via mask to the topmost metal layer in the structure, that is, the bottom metal layer in the top tier, as seen in Figure 7-1. The top metal has openings that serve as self-aligned masks during the etching process. After the oxide is etched, a Ti/TiN liner is deposited from a collimated biased-sputter source, tungsten (W) plugs are formed by CVD ( $475^{\circ}\text{C}$ ) to connect the two metal layers, and excess W is removed by CMP. Additional tiers can be bonded and interconnected by repeating the process.

Three-tier via chains were fabricated and interconnected with concentric vias. Each tier contained one layer of metal with deposited oxide layers of sufficient thickness to simulate a completed CMOS circuit stack. Each cycle of the chains consisted of a connection from the top tier to the middle tier down to the bottom tier and back up to the top. A scanning electron micrograph of a cross section of the structure is shown in Figure 7-5. A voltage sweep of 0–100 mV (at a compliance of  $100\text{ }\mu\text{A}$ ) was applied across the entire chain length to measure the chain resistance, and all current-voltage characteristics obtained were linear. Figure 7-6 is a plot of the data from one wafer for three sizes of vias tested. The resistance per via shown on the plot is the chain resistance divided by the number of vias in the chain (6936).

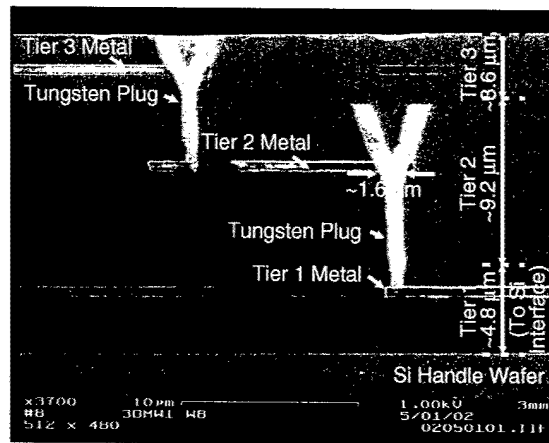


Figure 7-5. Scanning electron micrograph cross section of concentric vias in an oxide-bonded structure. The via etch created a sloped profile above the holes in the metal that were not completely filled with tungsten, producing "Y" shaped plugs in cross section.

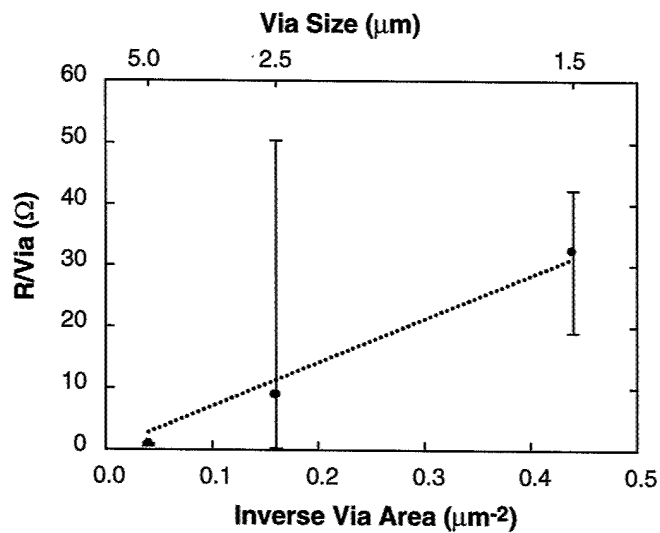


Figure 7-6. Plot of mean via resistance and range for three-tier via chains. Via size refers to the width of the opening in the top metal.



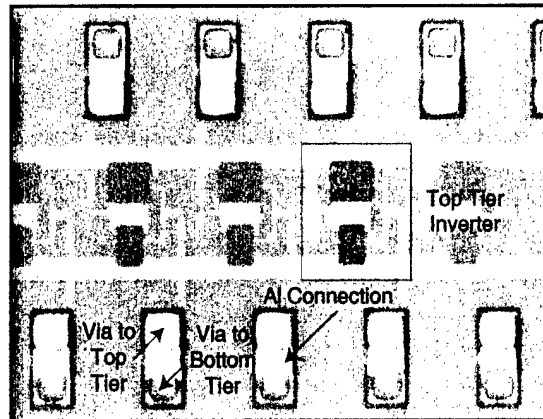


Figure 7-7. Photograph of section of a three-dimensional (3D) ring oscillator. The W plug concentric via process was not used for this device.

Wafers fabricated using a 0.8- $\mu\text{m}$  SOI CMOS process [1] were aligned and oxide bonded as described above to form 3D ring oscillators. The output of an inverter on one level was connected to the input of the next inverter on the other level with aluminum since the design did not include concentric vias. A section of a ring oscillator is shown in Figure 7-7. The gate delay data in Figure 7-8 show that the circuit is functional, demonstrating that the bonding process is compatible with completed devices.

In summary, 3D integrated circuits have been fabricated using a low-temperature oxide bonding technique that can be applied to completed circuit wafers. Two-tier SOI CMOS circuits had operational ring oscillators, and three-tier concentric via chains were functional at sizes as small as 1.5  $\mu\text{m}$ . The three-tier structure also showed that the oxide bonding technique could be extended to several circuit layers by simply repeating the process. These results clearly demonstrate that the technology has the potential to be useful in a variety of very large scale integrated circuit architectures.

K. Warner	J. Burns
S. Cann	C. Keast
R. Kunz	D. Lennon
A. Loomis	W. Mowers
P. Nitishin	D. Yost

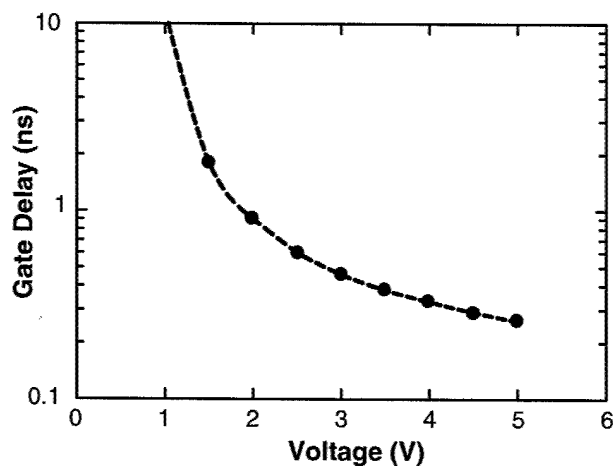


Figure 7-8. Gate delay vs voltage for a 65-stage ring oscillator fabricated in 0.8- $\mu\text{m}$  CMOS with 3- $\mu\text{m}$  3D vias.

#### REFERENCES

1. J. Burns, L. McIlraith, C. Keast, C. Lewis, A. Loomis, K. Warner, and P. Wyatt, *IEEE International Solid-State Circuits Conference Digest of Technical Papers* (IEEE, Piscataway, N.J., 2001), p. 268.
2. Q.-Y. Tong, T.-H. Lee, W.-J. Kim, T. Y. Tan, U. Gösele, H.-M. You, W. Yun, and J. K. O. Sin, *IEEE International SOI Conference Proceedings* (IEEE, Piscataway, N.J., 1996), p. 36.
3. R. Stengl, T. Tan, and U. Gösele, *Jpn. J. Appl. Phys.* **28**, 1735 (1989).
4. Q.-Y. Tong and U. Gösele, *Electrochemical Society Proceedings*, Vol. 95-7 (Electrochemical Society, Pennington, N.J., 1995), p. 78.
5. W. P. Maszara, G. Goetz, A. Caviglia, and J. B. McKitterick, *J. Appl. Phys.* **64**, 4943 (1988).

7

6

4

3

## REPORT DOCUMENTATION PAGE

**Form Approved**  
**OMB No. 0704-0188**

Public reporting burden for this collection of information is estimated to average 1 hour per response, including the time for reviewing instructions, searching existing data sources, gathering and maintaining the data needed to complete and reviewing the collection of information. Send comments regarding this burden estimate or any other aspect of this collection of information, including suggestions for reducing this burden, to Washington Headquarters Services, Directorate for Information Operations and Reports, 1215 Jefferson Davis Highway, Suite 1204, Arlington, VA 22202-4302, and to the Office of Management and Budget, Paperwork Reduction Project (0704-0188), Washington, DC 20503.

[illegible]